Sustained ErbB activation causes demyelination and hypomyelination by driving necroptosis of mature oligodendrocytes and apoptosis of oligodendrocyte precursor cells

Abbreviated title: ErbB overactivation causes white matter lesions

Authors: Xu Hu,[1,†] Guanxiu Xiao,[1,†] Li He,[1,†] Xiaojie Niu,[1] Huashun Li,[1] Tianjie Lou,[1] Qianqian Hu,[1] Youguang Yang,[1] Qi Xu,[1] Zhengdong Wei,[1] Mengsheng Qiu,[1] Kenji F. Tanaka,[2] Ying Shen,[3] and Yanmei Tao[1,*]

Affiliations:

[1]Key Lab of Organ Development and Regeneration of Zhejiang Province, Institute of Life Sciences, College of Life and Environmental Sciences, Hangzhou Normal University, Hangzhou 310000, China.

[2]Department of Neuropsychiatry, Keio University School of Medicine, Tokyo 160-8582, Japan.

[3]Department of Neurobiology, Key Laboratory of Medical Neurobiology of Zhejiang Province, Zhejiang University School of Medicine, Hangzhou 310058, China.

[†]These authors contributed equally.

Corresponding Author: [*]Correspondence and requests for materials should be addressed to Y.T. (e-mail: ytao@hznu.edu.cn)

Number of pages: 61

Numbers of figures: 9 main figures; 6 Extended data figures

Numbers of words for abstract, introduction, and discussion (separately): 248, 624, 1593

Conflict of interest: The authors declare no competing interests.

Acknowledgments

We thank Haiping Xiong, Wanwan He, Kaiwei Zhang, and Shasha Zhang in Hangzhou Normal University for the assistance in EM image analyses. This work was supported by grants from the National Natural Science Foundation of China (31371075, 31671070, and 31871030 to YT).

Abstract

Oligodendrocytes are vulnerable to genetic and environmental insults and its injury leads to demyelinating diseases. The roles of ErbB receptors in maintaining the CNS myelin integrity are largely unknown. Here we overactivate ErbB receptors that mediate signaling of either neuregulin or EGF family growth factors and found their synergistic activation caused deleterious outcomes in white matter. Sustained ErbB activation induced by the tetracycline-dependent mouse tool *Plp*-tTA resulted in demyelination, axonal degeneration, oligodendrocyte precursor cell (OPC) proliferation, astrogliosis, and microgliosis in white matter. Moreover, there was hypermyelination prior to these inflammatory pathological events. In contrast, sustained ErbB activation induced by another tetracycline-dependent mouse tool *Sox10*$^{+/rtTA}$ caused hypomyelination in the corpus callosum and optic nerve, which appeared to be a developmental deficit and did not associate with OPC regeneration, astrogliosis, or microgliosis. By tracing the differentiation states of cells expressing tTA/rtTA-dependent transgene or pulse-labeled reporter proteins *in vitro* and *in vivo*, we found that *Plp*-tTA targeted mainly mature oligodendrocytes (MOs), whereas *Sox10*$^{+/rtTA}$ targeted OPCs and newly-formed oligodendrocytes. The distinct phenotypes of mice with ErbB overactivation induced by *Plp*-tTA and *Sox10*$^{+/rtTA}$ consolidated their non-overlapping targeting preferences in the oligodendrocyte lineage, and enabled us to demonstrate that ErbB overactivation in MOs induced necroptosis that caused inflammatory demyelination, whereas in OPCs induced apoptosis that caused non-inflammatory hypomyelination. Early interference with aberrant ErbB activation ceased oligodendrocyte deaths and restored myelin development in both mice. This study suggests

57 that aberrant ErbB activation is an upstream pathogenetic mechanism of demyelinating
58 diseases, providing a potential therapeutic target.
59
60 **Significance statement:**
61 Primary oligodendropathy is one of the etiological mechanisms for multiple sclerosis, and
62 oligodendrocyte necroptosis is a pathological hallmark in the disease. Moreover, the
63 demyelinating disease is now a broad concept that embraces schizophrenia, in which white
64 matter lesions are an emerging feature. ErbB overactivation has been implicated in
65 schizophrenia by genetic analysis and postmortem studies. This study suggests the
66 etiological implications of ErbB overactivation in myelin pathogenesis and elucidates the
67 pathogenetic mechanisms.

68 **Introduction**

69 Oligodendrocytes form myelin to speed up the axonal impulse conduction while supporting
70 neuronal function and integrity in the central nervous system (CNS). White matter is
71 expanded, with a growth peak during juvenile to adolescence, by oligodendrocyte
72 precursor cell (OPC) proliferation. Terminally differentiated OPCs differentiate into
73 newly-formed oligodendrocytes (NFOs) under stringent regulation by extrinsic and
74 intrinsic signals (Bergles and Richardson, 2015; Emery and Lu, 2015). NFOs progress from
75 pre-myelinating oligodendrocytes to newly myelinating oligodendrocytes. Myelinating
76 oligodendrocytes effectively generate myelin sheaths in a short time window. After myelin
77 formation, mature oligodendrocytes (MOs) are extremely stable in maintaining myelin
78 sheaths (Watkins et al., 2008; Czopka et al., 2013; Xiao et al., 2016; Tripathi et al., 2017;
79 Hughes et al., 2018). However, a plethora of factors, including genetic alteration,
80 inflammatory mediators, ischemia, trauma, viruses, and toxins, can damage
81 oligodendrocytes and result in demyelinating diseases (Bradl and Lassmann, 2010).
82 Understanding the pathogenetic mechanisms is essential for developing strategies to
83 combat myelin loss and promote myelin restoration.

84 Intracellular signaling pathways, such as MAPK, Akt, and mTOR, are activated to
85 promote oligodendrocyte differentiation, survival, and myelination (Flores et al., 2000;
86 Flores et al., 2008; Ishii et al., 2012; Bercury et al., 2014). Tyrosine kinase receptors
87 ErbB(1-4), mediating abovementioned signal transduction pathways, are known to be
88 fundamental to various neural developmental events (Mei and Nave, 2014). Numerous
89 growth factors are able to activate ErbB receptors, including the neuregulin (NRG) family
90 (NRG1-NRG6) and the epidermal growth factor (EGF) family (EGF, HB-EGF, TGFα,

91 amphiregulin, epiregulin, β-cellulin, and epigen). Among them, most of the EGF family
92 ligands bind to EGFR only, and the NRG family ligands bind to ErbB3 and ErbB4, except
93 that HB-EGF, β-cellulin, and epiregulin can bind both EGFR and ErbB4 (Mei and Nave,
94 2014). Ligand binding stimulates ErbB receptors to dimerize with one another or
95 preferentially with ErbB2, activating multiple downstream signaling pathways (Mei and
96 Nave, 2014).

97 Although it is well-established that ErbB2 and ErbB3 are crucial to peripheral myelin
98 development (Nave and Salzer, 2006), the roles of ErbB receptors in oligodendrocytes have
99 long been debated. For example, ErbB3 has been reported to be dispensable for
100 oligodendrocyte development (Schmucker et al., 2003), and ErbB3/ErbB4 double
101 knockout from embryonic age does not result in CNS myelin alteration (Brinkmann et al.,
102 2008). However, there is another report that ErbB3 depletion in oligodendrocytes from
103 postnatal day 19 (P19) results in adult hypomyelination (Makinodan et al., 2012). Studies
104 on oligodendrocyte-specific knock-out mice have validated the expression of ErbB3 and
105 ErbB4 in oligodendrocytes (Brinkmann et al., 2008), while phosphorylated EGFR is
106 detected in oligodendrocytes by immunostaining (Palazuelos et al., 2014). Despites the
107 controversial results from loss-of-function studies, overexpressing NRG1 Type I or Type
108 III in neurons, or hEGFR in oligodendrocytes (*CNP*-hEGFR), promotes the CNS
109 myelination (Aguirre et al., 2007; Brinkmann et al., 2008). Interestingly, transgenic mice
110 *CNP*-hEGFR increases the numbers of myelinated axons but not myelin thickness (Aguirre
111 et al., 2007), whereas NRG1-overexpressing mice exhibit hypermyelination of individual
112 axons (Brinkmann et al., 2008). These results suggest that EGF-ErbB and NRG-ErbB
113 receptors play different roles in oligodendrocytes. However, the possible synergistic effects

of overactivating NRG-ErbB and EGF-ErbB receptors in oligodendrocytes have not been investigated.

To understand the consequences of co-activating ErbB receptors in oligodendrocytes, we employed a pan-ErbB strategy and activated endogenous ErbB receptors mediating either NRG or EGF signaling in oligodendrocytes. The results demonstrated that overactivating ErbB receptors in oligodendrocytes caused deleterious outcomes in white matter. Further, with the finding that the two inducible mouse tools, *Plp*-tTA and *Sox10*$^{+/rtTA}$, differentially targeted MO and OPC-NFO stages, we demonstrated that ErbB overactivation induced primary MO necroptosis and OPC apoptosis, causing inflammatory demyelination and non-inflammatory hypomyelination, respectively. Early interference with the aberrant activation of ErbB signaling was effective to cease these pathological progressions and restore oligodendrocyte numbers and myelin development.

Materials and Methods

Animals. *Plp*-tTA transgenic mice were from the RIKEN BioResource Center (Stock No. RBRC05446). Transgenic mice *TRE*-ErbB2^{V664E} (Stock No. 010577) was from the Jackson Laboratory. Sox10$^{+/rtTA}$ mice were from Dr. Michael Wegner (University Erlangen-Nurnberg, Germany). Unless otherwise indicated, mice were housed in a room with a 12-hour light/dark cycle with access to food and water *ad libitum*. For biochemical and histological experiments, *Plp*-tTA;*TRE*-ErbB2^{V664E} (*Plp*-ErbB2^{V664E}) and *Sox10*$^{+/rtTA}$;*TRE*-ErbB2^{V664E} (*Sox10*-ErbB2^{V664E}) mice with either sex and their littermate

control mice with matched sex were used. Animal experiments were approved by the Institutional Animal Care and Use Committee of the Hangzhou Normal University. For genotyping, the following primers were used: for *Plp*-tTA (630bp), PLPU-604 5'-TTT CCC ATG GTC TCC CTT GAG CTT, mtTA24L 5'-CGG AGT TGA TCA CCT TGG ACT TGT; for Sox10$^{+/rtTA}$ (618bp), sox10-rtTA1 5'-CTA GGC TGT CAG AGC AGA CGA, sox10-rtTA2 5'-CTC CAC CTC TGA TAG GT CTT G; for *TRE*-ErbB2^{V664E} (625bp), 9707 5'-AGC AGA GCT CGT TTA GTG, 9708 5'-GGA GGC GGC GAC ATT GTC.

Tet-Off or Tet-On treatment of mice. Mice with Tet-system contain genes of tetracycline-controlled transcriptional activator (tTA) or reverse tetracycline-controlled transcriptional activator (rtTA) driven by cell-specific promoters. When fed with Dox, these mice are able to switch on or off expression of a gene under the control of *tetracycline-responsive element* (*TRE*), specifically in rtTA- or tTA-expressing cells, which are called 'Tet-on' or 'Tet-off', respectively. The offspring of *Sox10*$^{+/rtTA}$ during the indicated periods were fed with Dox (2 mg/mL × 10 mL/day from P21 to indicated test day) in drinking water to induce the expression of ErbB2^{V664E} in *Sox10*-ErbB2^{V664E} mice (Tet-On). For the offspring of *Plp*-tTA, Dox was given (Tet-off) from the embryonic day (through pregnant mothers) to their weaning day at P21 to inhibit the expression of ErbB2^{V664E} during this period in *Plp*-ErbB2^{V664E} mice (0.5 mg/mL × 10 mL/day of Dox before P21). Water bottles were wrapped with foil to protect Dox from light. All used littermate control mice were treated the same.

160 **Stereotaxic injection of AAV viruses.** pAAV-*TRE*-EYFP plasmids (Addgene) were
161 packaged as AAV2/9 viruses, and produced with titers of 2.0E+13 particles per mL by
162 OBio (Shanghai, China). Mice were anesthetized by 1% pentobarbital (50 mg/kg, i.p.) and
163 mounted at stereotaxic apparatus (RWD68025). AAV-*TRE*-EYFP (2 μL) was injected into
164 the corpus callosum (from bregma in mm, M-L: ±1.2, A-P: +0.5, D-V: -2.2) under the
165 control of micropump (KDS310) at a speed of 0.05 μL/min. Injecting needles (Hamilton
166 NDL ga33/30 mm/pst4) were withdrawn 10 min after injection. Infected brains were
167 isolated 1 or 2 days later and brain slices were immunostained with anti-GFP antibody to
168 enhance the visualization of the reporter protein.
169
170 **Electron Microscopy.** Mice were anesthetized and transcardially perfused with 4%
171 sucrose, 4% paraformaldehyde (PFA) and 2% glutaraldehyde in 0.1 M phosphate buffer
172 (PB, pH 7.4). The brains and optic nerves were isolated carefully. The corpora callosa and
173 prefrontal cortices were further dissected carefully under stereoscope. Tissues were post-
174 fixed overnight at 4°C in 1% glutaraldehyde in 0.1 M PB. 24 h later, samples were washed
175 by 0.1 M PB and osmicated with 2% osmium tetroxide 30-60 min at 4°C, washed by 0.1
176 M PB and by deionized H_2O at 4°C, and dehydrated in graded (50-100%) ethanol. Samples
177 were incubated with propylene oxide and embedded with embedding resins. Ultrathin
178 sections were stained with 2% uranyl acetate at 4°C for 30 min, and then photographed
179 with Tecnai 10 (FEI). EM images were analyzed by ImageJ (NIH). To eliminate the bias
180 on circularity, *g*-ratio of each axon was calculated by the perimeter of axons (inner) divided
181 by the perimeter of corresponding fibers (outer). Axonal diameters were normalized by
182 perimeters through equation: diameter = perimeter/π. This procedure allows for inclusion

183 of irregularly shaped axons and fibers and helps to eliminate biased measurement of
184 diameters based on circularity. For quantitative analysis, cross sections of each neural
185 tissue were divided into 5 areas, and more than two images, randomly selected from each
186 area, were examined. The g-ratio of detectable myelinated axons in these images was
187 measured. The numbers of detectable axons from each mouse were not the same. *g*-ratio
188 from all detectable axons of one mouse was averaged and averaged *g*-ratio of three to five
189 mice were used for statistical analysis.
190
191 **Immunofluorescence staining.** Deeply anesthetized mice were transcardially perfused
192 with 0.01 M PBS and then 4% PFA in 0.01 M PBS. Mouse brains were isolated and post-
193 fixed in 4% PFA in 0.01 M PBS overnight at 4 °C, and then transferred into 20% and
194 subsequently 30% sucrose in PBS overnight at 4 °C. Brains were then embedded in OCT
195 (Thermo Fisher scientific) and sectioned into 20 μm on a cryostat sectioning machine
196 (Thermo Fisher scientific, Microm HM525). Brain slices were incubated with a blocking
197 buffer (10% fetal bovine serum and 0.2% Triton-X-100 in 0.01 M PBS) for 1 h at room
198 temperature (RT), and then incubated at 4 °C overnight with primary antibodies diluted in
199 the blocking buffer. The primary antibodies used were: GFP (1:500, Abcam, ab13970),
200 CC1 (1:500, Abcam, ab16794), NG2 (1:200, Abcam, ab50009), Ki67 (1:400, Cell
201 Signaling Technology, 9129), GFAP (1:2000, Millipore, MAB360), Iba1 (1:1000,
202 Millipore, MABN92), MBP (1:100, Millipore, MAB382), TCF4 (1:500, Millipore, 05-
203 511), Olig2 (1:500, Millipore, AB9610), TUJ1 (1:500, Sigma, T5076), RIP3 (1:500, QED,
204 2283), MLKL (1:500, Abgent, AP14272B). After washing three times with 0.1% Triton-
205 X-100 in 0.01 M PBS, samples were incubated at RT for 1 h with Alexa-488 or -594

206 secondary antibody, and then washed and mounted on adhesion microscope slides
207 (CITOTEST) with fluorescent mounting medium. Nuclear labeling was completed by
208 incubating slices with DAPI (0.1 μg/mL, Roche) at RT for 5 min after incubation with
209 secondary antibodies. Except for the antibody against NG2, antigen retrieval in 0.01 M
210 sodium citrate buffer (pH 6.0) at 80-90 °C for 10 min was necessary before primary
211 antibody incubation for brain slices to achieve definitive signals. Images were taken by a
212 Zeiss LSM710 confocal microscope or a Nikon Eclipse 90i microscope. For cell counting
213 based on immunostaining results, soma-shaped immunoreactive signals associated with a
214 nucleus was counted as a cell. The immunostaining intensity was measured by ImageJ with
215 background subtraction. Averaged intensity of areas with MBP signals was calculated as
216 MBP intensity and normalized to that of controls. For MBP distribution analysis, images
217 were applied with a threshold to eliminate the background, and the percentage of signal
218 area in the total area was quantified as the signal distribution and normalized to that of
219 controls.
220
221 **Luxol fast blue (LFB) staining.** Brain slices were obtained as described in
222 Immunofluorescence staining. After sufficient washing with 0.01 M PBS, the slices were
223 transferred into a mixture of trichloromethane and ethanol (volume ratio 1:1) for 10 min
224 and then 95% ethanol for 10 min. They were next incubated in 0.2% Luxol fast blue
225 staining solution (0.2 g Solvent blue 38, 0.5 mL acetic acid, 95% ethanol to 100 mL) at
226 60 °C overnight. The next day, tissues were incubated for 5 min each in turn in 95% ethanol,
227 70% ethanol and ddH_2O for rehydration, followed by incubation alternatively in 0.05%
228 Li_2CO_3, 70% ethanol and ddH_2O for differentiation until the contrast between the gray

229 matter and white matter became obvious. After that, tissues were incubated for 10 min each
230 in 95% and 100% ethanol to dehydrate, and then 5 min in dimethylbenzene to clear, before
231 quickly mounting with neutral balsam mounting medium (CWBIO). All steps were
232 operated in a ventilation cabinet. The LFB intensity in the corpus callosum was measured
233 by Image J with background subtraction, and normalized to that of controls.
234
235 **TUNEL assay.** Apoptotic cells were examined with terminal deoxynucleotidyl transferase
236 (TdT)-mediated deoxyuridine triphosphate (dUTP) nick-end labeling (TUNEL) assay
237 according to the manufacturer's instructions (Vazyme; Yeasen). In brief, brain slices which
238 were obtained as that described in Immunofluorescence staining were digested for 10 min
239 by proteinase K (20 μg/mL) at RT. After washing twice with PBS, brain slices were
240 incubated with Equilibration Buffer for 30 min at RT, and subsequently with Alexa Fluor
241 488-12-dUTP Labeling Mix for 60 min at 37°C. After washing with PBS three times, brain
242 slices were stained with DAPI before being mounted under coverslips. For co-labeling of
243 apoptotic nuclei in slices with immunofluorescence staining, TUNEL assay was performed
244 after washing of the secondary antibody.
245
246 **Western blotting.** Subcortical white matter tissues including the corpus callosum were
247 isolated and homogenized. Homogenates in lysis buffer (10 mM Tris-Cl, pH 7.4, 1% NP-
248 40, 0.5% Triton-X 100, 0.2% sodium deoxycholate, 150 mM NaCl, 20% glycerol, protease
249 inhibitor cocktail) at a ratio of 2 mL per 100 mg tissue were lysed overnight in 4°C. Lysates
250 were centrifuged at 12,000 g and 4°C for 15 min to get rid of the unsolved debris.
251 Concentration of the supernatant was measured by BCA assay. Proteins in samples were

252 separated by 6-12% SDS-PAGE, transferred to a Immobilon-P Transfer Membrane
253 (Millipore), and then incubated with indicated primary antibodies diluted in blocking
254 buffer at 4°C overnight after blocking by 5% non-fat milk solution in TBST (50 mM Tris,
255 pH 7.4, 150 mM NaCl, 0.1% Tween 20) for 1 h at RT. The primary antibodies used were:
256 pErbB3 (1:2500, Abcam, ab133459), pErbB4 (1:2500, Abcam, ab109273), pErbB2
257 (1:2500, Abgent, AP3781q), EGFR (1:5000, Epitomics, 1902-1), pEGFR (1:2500,
258 Epitomics, 1727-1), GAPDH (1:5000, Huabio, EM1101), MBP (1:1000, Millipore,
259 MAB382), ErbB3 (1:200, Santa Cruz Biotechnology, sc-285), ErbB4 (1:200, Santa Cruz
260 Biotechnology, sc-283), ErbB2 (1:200, Santa Cruz Biotechnology, sc-284), Akt (1:5000,
261 Cell signaling Technology, 9272), pAkt (1:3000, Cell signaling Technology, 9271), Erk1/2
262 (1:5000, Cell signaling Technology, 9102), pErk1/2 (1:5000, Cell signaling Technology,
263 4370), RIP3 (1:2000, QED, 2283), MLKL (1:2000, Abgent, AP14272B). For antibodies
264 against phosphorylated proteins, 10% fetal bovine serum was used as a blocking buffer.
265 Next day, the membranes were washed by TBST for three times and incubated with the
266 secondary antibodies for 1 h at RT. Membranes were washed again and incubated with
267 Immobilon Western Chemiluminescent HRPSubstrate (Millipore) for visualization of
268 chemiluminescence by exposure to X-ray films or Bio-Rad GelDOCXR^{+} Imaging System.
269 Intensities of protein bands were measured by ImageJ, and statistical analysis was
270 performed after subtraction of the background intensity and normalization with controls in
271 each batch of experiments.
272
273 **OPC cultures and differentiation *in vitro*.** The cortices of mice at P2–P5 were isolated
274 and sheared into pieces, and digested by 0.25% Trypsin in $Ca2^{+}Mg2^{+}$-free D-Hanks for 30

min at 37 °C. Trypsinized tissues were triturated and passed through 40 μm mesh. OPCs were obtained from the dissociated cells using MS Columns (Miltenyi Biotec 130-042-201) with magnetic beads (Miltenyi Biotec 130-101-547) to positively select PDGFRα^{+} cells according to the manufacturer's recommendations. Isolated OPCs were plated into a poly-L-lysine-coated glass coverslips at a density of 20,000 cells per cm^{2} with DMEM/F12 supplemented with 10% fetal bovine serum. Four hours later, the medium was replaced with DMEM/F12 medium with 2% B27, 20 ng/mL bFGF and 10 ng/mL PDGFAA. For differentiation induction, the medium was replaced with DMEM/F12 medium with 2% B27 and 40 ng/mL triiodothyronine. For cells from *Sox*-ErbB2^{V664E} mice, 3 μg/mL Dox was added into the medium 24 h after plating.

Statistical Analysis. All data were analyzed using Prism (Graphpad) and presented as mean ± s.e.m.. Unpaired two-tailed Student's *t* test was used for analysis between two groups with one variable. Statistical significance was set at $*P < 0.05$, $**P < 0.01$, $***P < 0.001$. For western blotting and staining results, statistical analyses were performed after subtraction of the background intensity and normalization with controls in each batch of experiments to minimize the influences of batch-to-batch variations. Detailed statistical information for each experiment was included in the figure legends.

298 **Results**

299 **ErbB overactivation caused inflammatory demyelination in *Plp*-ErbB2^{V664E} mice**

300 To manipulate ErbB receptor activities specifically in oligodendrocytes *in vivo*, we
301 employed tetracycline-controlled systems whose induction or blockade depends on the
302 presence of doxycycline (Dox). We generated *Plp*-tTA;*TRE*-ErbB2^{V664E} (*Plp*-ErbB2^{V664E})
303 bi-transgenic mice by crossing *Plp*-tTA with *TRE*-ErbB2^{V664E} mice. Breeding pairs, as well
304 as their offspring, were fed with Dox to 'Tet-off' the *TRE*-controlled transcription. Dox
305 was withdrawn when the offspring were weaned on P21 (Fig. 1*A*). Among ErbB1-4
306 receptors, ErbB2 that does not bind to any known ligand is the preferred partner to other
307 ligand-bound ErbB members. ErbB2^{V664E} contains an amino acid mutation (Vla_{664}/Glu_{664})
308 within the transmembrane domain facilitating its dimerization with other ErbB receptors
309 and potentiating their downstream signaling (Chen et al., 2017). ErbB2^{V664E} expression
310 was significantly induced in the white matter of *Plp*-ErbB2^{V664E} mice within 1 day post
311 Dox-withdrawal (dpd) (Fig. 1*B*). Notably, *Plp*-ErbB2^{V664E} mice around P35 exhibited
312 severe ataxia while walking on a grid panel (Fig. 1*C*). Moreover, *Plp*-ErbB2^{V664E} mice
313 showed difficulty in rolling over, indicating severely impaired motor coordination. This
314 was unexpected as this phenotype has not been reported for NRG1- or hEGFR-
315 overexpressing mice (Aguirre et al., 2007; Brinkmann et al., 2008).

316 In *Plp*-ErbB2^{V664E} mice at P21 before Dox withdrawal, activities of endogenous ErbB
317 receptors and the downstream Akt and Erk (MAPK) in white matter were not altered
318 (Extended data Fig. 1-1*A*). In *Plp*-ErbB2^{V664E} mice at P35 with 14 dpd, with the expression
319 and phosphorylation of ectopic ErbB2^{V664E}, endogenous ErbB receptors in the white matter,
320 including both EGFR that mediates EGF signaling and ErbB3/ErbB4 that mediate NRG

321 signaling, were strikingly phosphorylated and activated (Fig. 1*D*, *E*). Activating ErbB
322 receptors stimulated downstream signaling including both Erk and Akt, as their
323 phosphorylation significantly increased in the white matter of *Plp*-ErbB2^{V664E} mice (Fig.
324 1*D*, *E*).

325 Overactivation of ErbB receptors caused lower myelin staining intensity as exhibited
326 in the corpus callosum of *Plp*-ErbB2^{V664E} mice at 9 dpd after Luxol fast blue (LFB) staining
327 (Fig. 1*F*). White matter tracts in the lateral part of corpus callosum of *Plp*-ErbB2^{V664E} mice
328 at 9 dpd were obviously fragmented (black arrows). Notably, at 14 dpd, myelin loss became
329 more evident throughout the corpus callosum, as that LFB staining intensities dropped
330 dramatically in both the middle and lateral parts (Fig. 1*F*). Immunostaining of myelin basic
331 protein (MBP) also revealed dramatic myelin loss in the corpus callosum at 14 dpd (Fig.
332 1*F*), suggesting that *Plp*-ErbB2^{V664E} mice were undergoing CNS demyelination after Dox
333 withdrawal. Western blotting revealed that the induced ErbB2^{V664E} expression was
334 associated with MBP loss in multiple brain regions of *Plp*-ErbB2^{V664E} mice (Fig. 1*G*),
335 indicating a global CNS demyelination. Indeed, the electron microscopic (EM)
336 examination revealed that myelin sheaths of some axons in *Plp*-ErbB2^{V664E} mice ruptured
337 or underwent breakdown (Fig. 1*H*, *I*, *J*). Due to demyelination, only a few intact axons
338 were detected in the midline of the corpus callosum of *Plp*-ErbB2^{V664E} mice at 14 dpd (Fig.
339 1*I*, *J*). When axonal tracts in the corpus callosum of *Plp*-ErbB2^{V664E} mice at 14 dpd were
340 immunostained by TuJ1, the antibody recognizing neuronal specific β-tubulin III, the
341 immunoreactivity dramatically reduced (Fig. 1*K*). Inflammatory demyelination is usually
342 complicated and aggravated by the pathological responses from nearby astrocytes and
343 microglia (Bradl and Lassmann, 2010; Burda and Sofroniew, 2014). Indeed, in the white

344 matter of *Plp*-ErbB2^{V664E} mice, astrogliosis and microgliosis were revealed after Dox
345 withdrawal (Extended data Fig. 1-1*B*, *C*; Fig. 1*L*, *M*). It was likely that inflammation
346 exacerbated myelin degradation and axon degeneration in the corpus callosum, given the
347 fact that most axons were preserved in the optic nerves where inflammatory status, as
348 indicated by transcription of GFAP and pro-inflammatory cytokine IL-1β, was
349 significantly milder than that in the corpus callosum of the same mice at 14 dpd (Fig. 1*N*).
350

351 **_Plp_-ErbB2^{V664E} white matter exhibited hypermyelination prior to demyelination**

352 Interestingly, despite the demyelination, the detectable axons, throughout the corpus
353 callosum, optic nerve, and prefrontal cortex in *Plp*-ErbB2^{V664E} mice, were hypermyelinated
354 (Fig. 1*I*). Myelinated axons detected in the brain of *Plp*-ErbB2^{V664E} mice had significantly
355 smaller *g*-ratio (axon diameter/fiber diameter), a quantitative indication of myelin
356 thickness for individual axons with different diameters (Fig. 1*I*). Myelin thickness showed
357 no difference between *TRE*-ErbB2^{V664E} and littermate *Plp*-tTA, two single transgenic
358 control mice, after Dox withdrawal (Extended data Fig. 1-2*A*). Therefore,
359 hypermyelination of detectable axons in *Plp*-ErbB2^{V664E} mice was a result of ErbB
360 signaling overactivation.

361 Hypermyelination of individual axons in *Plp*-ErbB2^{V664E} mice phenocopied that
362 observed in NRG1-overexpressing mice (Brinkmann et al., 2008), as well as that in the
363 transgenic mice with Akt or Erk signaling overactivation in oligodendrocytes (Harrington
364 et al., 2010; Ishii et al., 2013). We immunostained MBP in *Plp*-ErbB2^{V664E} mice, and found
365 that myelin structures and distributions remained mostly normal in the middle part of
366 corpus callosum at 9 dpd (Fig. 2*A*, inset 2' *vs* inset 2), despite that MBP loss and myelin

367 fragmentation were prominent at the cortical projection tips in the same mice (Fig. 2*A*, *C*).
368 An examination of the ultrastructure in these mice by EM revealed similar results that most
369 axons were intact in the midline of the corpus callosum, although they have been
370 significantly hypermyelinated (Fig. 2*B*, *D*). These results confirmed that hypermyelination
371 occurred early in *Plp*-ErbB2^{V664E} mice, consistent with the reported function of ErbB
372 signaling overactivation (Brinkmann et al., 2008; Harrington et al., 2010; Ishii et al., 2013).
373 Overactivation of ErbB receptors activates multiple downstream signaling, and transduce
374 more active intracellular signaling than transduction through the increase of ligands. Rapid
375 demyelination and axonal degeneration after 9 dpd may be attributed to inflammation that
376 exacerbated the pathological progression in *Plp*-ErbB2^{V664E} mice (Burda and Sofroniew,
377 2014).
378

379 **ErbB overactivation induced oligodendrocyte degeneration but OPC regeneration in**
380 ***Plp*-ErbB2^{V664E} mice**

381 To investigate the pathological mechanism, we examined the post-mitotic
382 oligodendrocytes by immunostaining with antibody CC1, and found a decreasing number
383 of intact CC1^{+} cells in the corpus callosum of *Plp*-ErbB2^{V664E} mice starting from 6 dpd
384 (Fig. 3*A*, *C*). Meanwhile, OPC (NG2^{+}Olig2^{+}) numbers were dramatically increased (Fig.
385 3*B*, C). These disproportionate oligodendrocyte lineage state changes were consistent with
386 the previous reports that demyelination induces OPC regeneration (Aguirre et al., 2007;
387 Bradl and Lassmann, 2010). We examined OPC proliferation by co-immunostaining for
388 Olig2 and Ki67, the proliferation marker. In normal condition after early development,
389 most proliferative OPCs (Ki67^{+}Olig2^{+}) resided in the subventricular zone, with a few in

390 the trunk of corpus callosum (Fig. 3*D*). In *Plp*-ErbB2^{V664E} mice starting from 6 dpd,
391 dramatic proliferation of OPCs was observed within the trunk of corpus callosum instead
392 of the subventricular zone (Fig. 3*D*, *E*), further indicating the pathogenetic state of myelin.
393 The non-specifically stained hemorrhagic spots (white asterisk) in the cortex of *Plp*-
394 ErbB2^{V664E} mice also indicated the inflammatory pathological status. The pathological
395 events, including myelin (MBP^{+}) breakdown, oligodendrocytes (CC1^{+}) degeneration, and
396 OPC (PDGFRα^{+}) regeneration, were also observed in *Plp*-ErbB2^{V664E} mice at P70 with 10
397 dpd (Extended data Fig. 3-1*A*-*E*). These pathological events were correlated with
398 inflammation as well (Extended data Fig. 3-1*F*-*H*), despite that the inflammatory profiles
399 (GFAP^{+} cell numbers reduced while Iba1^{+} cell numbers increased significantly in the
400 corpus callosum) were not the same as those in mice at P30 with 9 dpd (both GFAP^{+} and
401 Iba1^{+} cell numbers increased significantly). There were even more hemorrhagic spots
402 (white asterisk) in the cortex of adult *Plp*-ErbB2^{V664E} mice, indicating that the adult brains
403 were more vulnerable to inflammation. Therefore, ErbB overactivation induced by *Plp*-
404 tTA was detrimental to oligodendrocytes, causing inflammatory demyelination at both
405 adolescence and adulthood.
406

407 **ErbB overactivation caused oligodendrocyte number reduction and non-**
408 **inflammatory hypomyelination in *Sox10*-ErbB2^{V664E} mice**

409 Next, we examined the effects of ErbB overactivation on CNS myelin by a 'Tet-on' system
410 generated in *Sox10*$^{+/rtTA}$;*TRE*-ErbB2^{V664E} (*Sox10*-ErbB2^{V664E}) mice (Fig. 4*A*). ErbB2^{V664E}
411 expression was also significantly induced in the white matter within 1 day with Dox-
412 feeding (dwd), suggesting similarly prompt responses of tTA/rtTA transcription in *Sox10*-

413 ErbB2^{V664E} and *Plp*-ErbB2^{V664E} mice (Fig. 4*B*). *Sox10*-ErbB2^{V664E} mice with Dox feeding
414 from P21 developed severe motor dysfunction, including ataxia and tremors, and died
415 around P35. As a result, *Sox10*-ErbB2^{V664E} and littermate control mice were investigated
416 at P30 with 9 dwd. These mice had smaller body sizes at P30 and walked with difficulty
417 on a grid panel (Fig. 4*C*). Interestingly, *Sox10*-ErbB2^{V664E} mice performed normal rolling
418 over. Despite walking slowly in the grid walking test, *Sox10*-ErbB2^{V664E} mice did not
419 exhibit as many foot slips as *Plp*-ErbB2^{V664E} mice did. On the other hand, *Plp*-ErbB2^{V664E}
420 mice did not exhibit tremors. The tremors in *Sox10*-ErbB2^{V664E} mice should be ascribed to
421 the hypomyelination of peripheral nerves (Extended data Fig. 4-1*A*-*H*).

422 On P21 before Dox treatment, no ErbB2^{V664E} was detected in the white matter of
423 *Sox10*-ErbB2^{V664E} mice, indicating there was no leaky expression of the transgene.
424 Consistently, there were similar protein and phosphorylation levels of endogenous ErbB
425 receptors as well as downstream Akt and Erk (Extended data Fig. 1-1*D*). After 9 dwd,
426 western blotting revealed the expression and phosphorylation of ectopic ErbB2^{V664E}
427 accompanied with increases in phosphorylation of ErbB3 and ErbB4, but not that of EGFR,
428 in the white matter of *Sox10*-ErbB2^{V664E} mice (Fig. 4*D*, *E*). Even though only the activities
429 of ErbB3 and ErbB4, the receptors to the NRG family ligands, were increased in the white
430 matter of *Sox10*-ErbB2^{V664E} mice, both downstream Erk and Akt signaling were activated
431 (Fig. 4*D*, *E*). With the ErbB signaling overactivation, brain slices stained by LFB or
432 immunostained by MBP antibody exhibited lower staining intensity in the corpus callosum
433 of *Sox10*-ErbB2^{V664E} mice (Fig. 4*G*), consistent with the lower MBP levels detected by
434 western blotting (Fig. 4*D*, *F*). Unexpectedly, the examination of the ultrastructure of
435 *Sox10*-ErbB2^{V664E} white matter by EM did not find hypermyelination or myelin breakdown,

436 but revealed that the axons in the corpus callosum and optic nerve exhibited thinner myelin
437 with significantly increased *g*-ratio (Fig. 4*H*). *Sox10*$^{+/rtTA}$ is a knock-in mouse line, so that
438 the allele with *Sox10*-rtTA would not transcribe *Sox10* mRNA (Ludwig et al., 2004). We
439 analyzed the ultrastructure of myelinated axons in two control mice, *Sox10*$^{+/rtTA}$ and
440 littermate *TRE*-ErbB2^{V664E} mice, at P30 with 9 dwd and did not observe any differences
441 (Extended data Fig. 1-2*B*). Therefore, we can exclude the possible effect of
442 haploinsufficiency of Sox10 on late postnatal myelin development.

443 It is notable that in *Sox10*-ErbB2^{V664E} mice, the numbers of myelinated axons were not
444 altered (Fig. 4*I*), and myelin sheaths exhibited normal morphology (Fig. 4*H*). Moreover,
445 neither microgliosis nor astrogliosis was detected (Extended data Fig. 1-1*E*, *F*; Fig. 4*J*, *K*).
446 Consistently, there was no increases in pro-inflammatory cytokine (IL-1β and TNFα)
447 expression (Fig. 4*L*). Because there was no indication of inflammatory pathogenesis, we
448 can conclude that thinner myelin in *Sox10*-ErbB2^{V664E} white matter was caused by
449 developmental deficits not pathological conditions. Therefore, ErbB overactivation in
450 *Sox10*-ErbB2^{V664E} mice induced CNS hypomyelination rather than inflammatory
451 demyelination.

452 We further examined the states of oligodendrocytes and found the numbers of Olig2^{+},
453 NG2^{+}, and CC1^{+} cells all significantly decreased in the corpus callosum of *Sox10*-
454 ErbB2^{V664E} mice with 6 and more dwd (Fig. 5*A*-*C*). The number reduction of NG2^{+} and
455 CC1^{+} cells was proportional to each other and to that of Olig2^{+} cells, confirming that the
456 deficits in *Sox10*-ErbB2^{V664E} mice were development-dependent. OPC proliferation
457 decreased in the corpus callosum (Fig. 5*D*), further supporting that the oligodendrocyte
458 lineage states in *Sox10*-ErbB2^{V664E} white matter were different from that in *Plp*-ErbB2^{V664E}

459 white matter. As neither OPC nor oligodendrocyte differences were observed between
460 littermate *Sox10*$^{+/rtTA}$ and *TRE*-ErbB2^{V664E}, two control mice, at P30 with 9 dwd (Extended
461 data Fig. 5-1*A*,*B*), the developmental deficits in *Sox10*-ErbB2^{V664E} mice should be
462 attributed to ErbB overactivation in oligodendrocytes.
463

464 **_Plp_-tTA targeted mainly MOs whereas _Sox10_$^{+/rtTA}$ targeted OPC-NFOs**

465 To understand the cellular mechanisms of inflammatory demyelination (*Plp*-ErbB2^{V664E}
466 mice) and non-inflammatory hypomyelination (*Sox10*-ErbB2^{V664E} mice) induced by ErbB
467 overactivation, we had to first determine the cellular targeting preferences of Dox-
468 dependent transgenes in these two mouse models. The finding that *Plp*-ErbB2^{V664E} and
469 *Sox10*-ErbB2^{V664E} mice had few overlapping phenotypes was unexpected since that Sox10
470 is reported to express throughout the oligodendrocyte lineage, and *Sox10*$^{+/rtTA}$ knock-in
471 mice have been used to investigate all oligodendrocyte lineage cells (Wegener et al., 2015).
472 On the other hand, *Plp*-tTA transgenic mice have been reported to target MOs in the adult
473 brain (Inamura et al., 2012); however, *Plp* gene transcribes a shorter splicing isoform
474 DM20 in OPCs and NFOs during embryonic and early postnatal development (Trapp et al.,
475 1997). The previous report for *Sox10*$^{+/rtTA}$-targeting specificity was concluded by using
476 GFP reporter mice with Dox treatment for several weeks (Wegener et al., 2015). GFP is
477 highly stable with a ~26 h half-life (Corish and Tyler-Smith, 1999). In contrast,
478 transactivator tTA has a half-life less than 6.5 h (Chassin et al., 2019). Therefore, GFP
479 reporter generated in the original tTA/rtTA expressing cells can accumulate into the
480 following cellular stages when tTA/rtTA has degraded, and thus the reporter-containing
481 cells consist of tTA/rtTA-expressing cells and their progeny. In oligodendrocyte lineage,

482 terminal differentiated OPCs can differentiate into NFOs in as quickly as 2.5 h and NFOs
483 can mature in 1 day (Xiao et al., 2016). Because the induction of the 'Tet-on' or 'Tet-off'
484 system by Dox feeding or Dox withdrawal has a delayed effect on gene expression, to
485 examine the cellular targeting preferences under a condition with limited derivation from
486 original tTA/rtTA-expressing cells, we acutely delivered a *TRE*-controlled fluorescence
487 reporter carried by an adeno-associated virus (AAV) into the mouse brains at P14 or P35.
488 In these AAV-*TRE*-YFP-infecting mice, rtTA- or tTA-targeting cells were pulse-labeled,
489 allowing us to trace their differentiation states within a short time window.

490 *Plp*-tTA mice were raised with no Dox feeding, whereas *Sox10*$^{+/rtTA}$ were fed with Dox
491 for 3 days before the stereotaxic injection (Fig. 6*A*). One or 2 days after virus injection, the
492 reporter-containing (YFP^{+}) cells were all immunopositive for Olig2 in both mouse lines at
493 either age (Extended data Fig. 6-1*A*-*D*; Fig. 6*B*, C), confirming their oligodendrocyte
494 lineage specificity. To analyze the differentiation stage specificity, we immunostained
495 AAV-*TRE*-YFP infected brain slices with an antibody for NG2 or PDGFRα that labels
496 OPCs, or the antibody CC1 that labels post-mitotic oligodendrocytes. The results showed
497 that very few (4-7%) YFP^{+} cells were OPCs, while 92-97% of them were post-mitotic
498 oligodendrocytes in *Plp*-tTA mice 1 or 2 days after virus injection at either age (Fig. 6*B*,
499 *C*). In the case of *Sox10*$^{+/rtTA}$ mice at P14, little difference was observed as only 5-6% of
500 YFP^{+} cells were OPCs 1 or 2 days after virus injection (Fig. 6*B*). However, for *Sox10*$^{+/rtTA}$
501 mice at P35, approximately 26% of YFP^{+} cells were OPCs 1 day after virus injection (Fig.
502 6*C*). This observation excluded the possibility that the low OPC percentages in the
503 reporter-containing cells in *Sox10*$^{+/rtTA}$ mice at P14, or in *Plp*-tTA mice at both ages, were
504 due to selective infection by AAV. More intriguingly, the OPC/YFP^{+} cell ratio decreased

505 to 8% after 1 more day in *Sox10*$^{+/rtTA}$ mice at P35 (Fig. 6*C*). These results may suggest that
506 most of the pulse-labeled OPCs in *Sox10*$^{+/rtTA}$ mice at P35 were undergoing terminal
507 differentiation (tOPCs), and *Sox10*$^{+/rtTA}$ increasingly targeted tOPCs from P14 to P35.

508 In most cases from *Sox10*$^{+/rtTA}$ mice, we noticed the total numbers of NG2^{+}YFP^{+} (or
509 PDGFRα^{+}YFP^{+}) and CC1^{+}YFP^{+} cells were fewer than that of Olig2^{+}YFP^{+} cells (Fig. 6*C*),
510 which indicated the presence of reporter-containing cells that were neither positive for CC1
511 nor for NG2 (PDGFRα). These cells belong to the NFO stage, which includes both CC1^{-}
512 NG2^{-} (or CC1^{-}PDGFRα^{-}) and CC1^{+}NG2^{-} (or CC1^{+}PDGFRα^{-}) oligodendrocyte lineage
513 cells. The previous study for *Sox10*$^{+/rtTA}$-targeting specificity only examined the
514 PDGFRα/NG2 and CC1 immunoreactivities in reporter-containing cells. It is known that
515 most NFOs are also positive for CC1 immunostaining (Ye et al., 2009). The β-catenin
516 effector TCF4 is specifically expressed in the NFO stage (Fancy et al., 2009; Fu et al., 2009;
517 Ye et al., 2009), which was present in a subset of Olig2^{+} cells but absent in PDGFRα^{+} cells
518 in mice at P30 (Fig. 6*D*). In *Sox10*$^{+/rtTA}$ mice at P14, immunostaining revealed that
519 approximately 49% of YFP^{+} cells were NFOs (TCF4^{+}) 1 day after virus injection, but it
520 reduced to 28% after 1 more day (Fig. 6*E*, *G*). TCF4^{+} cells found in the corpus callosum at
521 P35 were far fewer than P14, and these cells appeared as clusters. Interestingly, in
522 *Sox10*$^{+/rtTA}$ mice at P35, YFP^{+} cells were mostly found in regions with TCF4^{+} cell clusters
523 (Extended data Fig. 6-1*E*), where approximately 56% of YFP^{+} cells were TCF4^{+} 1 day
524 after virus injection and it reduced to 29% after 1 more day (Fig. 6*F*, *G*). The half reduction
525 of NFO percentage in YFP^{+} cells from day 1 to day 2 was consistent with the previous
526 report that NFOs mature into MOs in 1 or 2 days (Xiao et al., 2016). There was another
527 possibility that the transcriptional activity of *Sox10*-rtTA was low in MOs, and thus took

528 more days to have detectable YFP levels. We analyzed the densities of TCF4^{+}YFP^{+} cells
529 and found that they reduced to half from day 1 to day 2 after viral infection in *Sox10*$^{+/rtTA}$
530 mice at either P14 or P35 (Fig. 6*H*). This result excluded the possibility that the reduction
531 of NFO ratio in YFP^{+} cells was due to the increase of targeted MOs, and confirmed the
532 maturation rate of pulse-labeled NFOs from day 1 to day 2. A similar transition rate is
533 applicable for targeted OPCs and NFOs from day 0 to day 1. Through analyses of the stage
534 alteration rate of reporter-containing cells from day 1 to day 2 after viral infection, we can
535 conclude that the *Sox10*$^{+/rtTA}$-targeting cells at day 0 should mostly be OPCs and NFOs.

536 YFP only have 4 amino-acid residue difference near the chromophore from GFP
537 (Wachter et al., 1998). Therefore, the YFP-containing MOs (CC1^{+}TCF4^{-}) in *Sox10*$^{+/rtTA}$
538 mice can be ascribed to the high stability of YFP. We have measured and reported that the
539 half-life of ErbB2 is ~8 h in HEK293 cells and ~9 h in breast cancer cells. Moreover, ligand
540 binding stimulates the turnover of ErbB receptors (Liu et al., 2007; Tao et al., 2009; Tao et
541 al., 2014). To clearly examine the oligodendrocyte stages with ErbB2^{V664E} expression, we
542 purified OPCs and induced transgene expression *in vitro*. ErbB2^{V664E} was visualized by
543 immunocytofluorescence in dissociated oligodendrocyte lineage cells from *Sox10*-
544 ErbB2^{V664E} mice, but not those from control mice, with Dox treatment (Fig. 7*A*).
545 Significant ErbB2 immunoreactivities were detected in OPCs (NG2^{+}) and NFOs (TCF4^{+})
546 (Fig. 7*B*, open white arrows). Essentially, there were only a few differentiated
547 oligodendrocytes with low MBP levels detected to have ErbB2 signals. Nevertheless,
548 ErbB2 signals in these MBP^{+} (low) cells, which just started maturation, became extremely
549 weak (Fig. 7*B*, solid white arrows). Once oligodendrocytes matured to have high MBP
550 levels, ErbB2 immunoreactivities disappeared (Fig. 7*B*, solid pink arrows), indicating that

551 there were no new ErbB2^{V664E} synthesis and the existed ErbB2^{V664E} degraded during
552 oligodendrocyte maturation. Despite a different oligodendrocyte stage proportion in the *in*
553 *vitro* system from that *in vivo*, we detected 67.1 ± 8.9 % ErbB2^{+} cells NG2^{+} (OPCs) from
554 the *Sox1*0-ErbB2^{V664E} cultures during early differentiation. Four days *in vitro* after
555 differentiation induction when many MBP^{+} cells were newly developed, 58.7 ± 4.0 %
556 ErbB2^{+} cells were TCF4^{+} (NFOs), and 18.1 ± 2.4 % were MBP^{+} (low) (Fig. 7*C*). There
557 were about 2.92 ± 1.8 % ErbB2^{+} were MBP^{+} (high) where minimal ErbB2 intensities were
558 detected (Fig. 7*C*, *D*). ErbB2 signals were highest in oligodendrocytes at OPC stage, and
559 close to zero at MO stage (Fig. 7*D*), consolidating the concept that ErbB2^{V664E} expression
560 induced by *Sox10*$^{+/rtTA}$ is mainly confined at OPC-NFO stages.

561 AAV-*TRE*-YFP in *Plp*-tTA mice also labeled some TCF4^{+} cells, which comprised
562 only 7-12% of YFP^{+} cells 1 or 2 days after virus injection at either age (Fig. 6*E*-*H*). It was
563 noticeable that *Plp*-tTA did not specifically target TCF4^{+} cell clusters in the corpus
564 callosum at P35 (Extended data Fig. 6-1*F*). These results implied that *Plp*-tTA did not
565 specifically target the OPC or NFO stage but randomly expressed in the OPC-NFO period
566 at a low ratio. Conversely, 90% of the YFP^{+} cells were TCF4^{-} and 92-97% were CC1^{+} in
567 *Plp*-tTA mice at either P14 or P35, suggesting that *Plp*-tTA steadily targeted MOs. Further,
568 the *in vitro* analyses validated this idea by showing that 96.7 ± 1.7 % MBP^{+} cells (Fig. 7*E*-
569 *G*), including both cells with low (Fig. 7*F*, solid white arrows) and high MBP levels (Fig.
570 7*F*, solid pink arrows) from the 'Tet-off' *Plp*-ErbB2^{V664E} mice, were ErbB2^{+}. There were
571 a few oligodendrocytes not MBP^{+}, corresponding to 5.29 ± 1.2 % NFOs (TCF4^{+}) with the
572 transgene expression (Fig. 7*F*, open white arrows). None of PDGFRα^{+} cells (OPCs) was
573 immunopositive for ErbB2 (Fig. 7*G*). Note the ErbB2 immunostaining intensities were

574 comparable in NG2^{+} cells from *Sox10*-ErbB2^{V664E} mice and MBP^{+} cells from *Plp*-
575 ErbB2^{V664E} mice (Fig. 7*D*), indicating comparable transactivation efficiencies of *Sox10*-
576 rtTA and *Plp*-rtTA at single cell levels. The *in vivo* and *in vitro* analyses corroborated that
577 *Sox10*$^{+/rtTA}$ and *Plp*-tTA target different oligodendrocyte differentiation stages (Fig. 7*H*),
578 which explains why ErbB overactivation induced distinct cellular and histological
579 phenotypes in *Plp*-ErbB2^{V664E} and *Sox10*-ErbB2^{V664E} mice.
580
581 **ErbB overactivation caused MO necroptosis whereas OPC apoptosis**
582 With the advantages of the non-overlapping phenotypes in *Plp*-ErbB2^{V664E} and *Sox10*-
583 ErbB2^{V664E} mice, we were able to investigate the pathogenetic mechanisms that determine
584 the different myelin responses in these two mouse models. MO number reduction occurred
585 earlier than the time when demyelination was obviously observed in the corpus callosum
586 of *Plp*-ErbB2^{V664E} mice, suggesting that primary oligodendropathy may be the cause of
587 demyelination. We noticed there was an increase in the numbers of nuclei associated with
588 CC1^{+} cell debris, starting from 6 dpd, in the corpus callosum of *Plp*-ErbB2^{V664E} mice (Fig.
589 3A, white arrows). We examined the corpus callosum of *Plp*-ErbB2^{V664E} mice by TdT-
590 mediated dUTP nick end labeling (TUNEL) assay, and observed as little apoptotic
591 signaling as that in controls (Fig. 8*A*-*C*). Immunostaining for cleaved caspase-3, the key
592 apoptotic signaling protein, also exhibited few signals there (Fig. 8*B,C*). These results
593 revealed that the degenerating CC1^{+} cells were necrotic rather than apoptotic. Consistently,
594 the oligodendrocyte nuclei associated with the destroyed myelin sheaths in *Plp*-ErbB2^{V664E}
595 mice were regular nuclei without apoptotic chromatin condensation (Fig. 1*H*, red asterisk).
596 In support of this theory, MLKL, the protein mediating oligodendrocyte necroptosis in

597 multiple sclerosis (Ofengeim et al., 2015) as well as the peripheral myelin breakdown after
598 nerve injury (Ying et al., 2018), demonstrated an increased expression in the callosal $CC1^+$
599 cells in *Plp*-ErbB2^{V664E} mice from 6 dpd (Fig. 8*D-F*). Necroptosis is a programmed form
600 of necrosis, and has been revealed to be a prominent pathological hallmark of multiple
601 sclerosis (Ofengeim et al., 2015). RIP3 is the kinase at the upstream of MLKL in this
602 programmed death signaling pathway (Sun et al., 2012; Ofengeim et al., 2015). Notably,
603 the expression of RIP3 was also elevated in the callosal $CC1^+$ cells in *Plp*-ErbB2^{V664E} mice
604 from 6 dpd as revealed by both immunostaining and western blotting (Fig. 8*D-F*).
605 Significant MLKL signals also appeared in the corpus callosum of adult *Plp*-ErbB2^{V664E}
606 mice at P70 with 10 dpd, indicating similar susceptibility of adult MOs to necroptosis
607 induced by ErbB overactivation (Extended data Fig.3-1*C,E*). Cell necroptosis is a trigger
608 to inflammation (Pasparakis and Vandenabeele, 2015). Based on the timeline, MO
609 necroptosis was the primary defect induced in *Plp*-ErbB2^{V664E} mice, followed by
610 inflammation, OPC regeneration, myelin breakdown, axonal degeneration, and other
611 pathological events as reported in multiple sclerosis (Bradl and Lassmann, 2010; Ofengeim
612 et al., 2015).

613 In contrast, for *Sox10*-ErbB2^{V664E} mice, a dramatic increase in cell apoptosis in the
614 corpus callosum was observed (Fig. 8*C*, *G*, *H*). These apoptotic nuclei, labeled either by
615 TUNEL assay or immunostaining of cleaved caspase-3, were localized in the $NG2^+$ and
616 $PDGFR\alpha^+$ cells (Fig. 8*I*), indicating apoptosis of OPCs. On the other hand, no increase of
617 MLKL or RIP3 was detected (Fig. 8*E*, *F*, *J*), indicating there was no necroptosis.
618 Developmental apoptosis does not arouse local inflammation, and hence no pathological
619 responses were observed in astrocytes and microglia in the white matter of *Sox10*-

620 ErbB2^{V664E} mice (Fig. 4*J*-*L*). It is also interesting to note that both the NG2^{+} cells with and
621 without TUNEL^{+} nuclei were hypertrophic in *Sox10*-ErbB2^{V664E} mice (Fig. 8*I*). This
622 phenomenon was not revealed for NG2^{+} cells in *Plp*-ErbB2^{V664E} mice (Fig. 3*B*), further
623 supporting that the OPC phenotypes in *Sox10*-ErbB2^{V664E} mice were attributed to the
624 transgene expression in OPCs.
625

626 **Early intervention ceased oligodendrocyte necroptosis/apoptosis and rescued**
627 **pathological phenotypes in both mice**

628 Next, we explored whether the pathological deficits induced by ErbB overactivation can
629 resolve after correcting the ErbB activities in oligodendrocytes. Toward this end, we
630 withdrew Dox for *Sox10*-ErbB2^{V664E} mice after 9 dwd or re-fed *Plp*-ErbB2^{V664E} mice with
631 Dox after 9 dpd. However, these mice were not rescued. Their disease conditions
632 progressed deleteriously as same as mice with continuous 'Tet-on' or 'Tet-off'. These
633 failures indicated that the pathology in both mice had progressed into an irreversible phase.
634 The delayed effects of Dox feeding or Dox withdrawal on 'Tet-on' or 'Tet-off' mice may
635 worsen the situations because that the real time for fully suppressing ErbB overactivation
636 was after 9 dwd or 9 dpd for *Sox10*-ErbB2^{V664E} and *Plp*-ErbB2^{V664E} mice. In contrast,
637 *Sox10*-ErbB2^{V664E} mice with 6 dwd, and *Plp*-ErbB2^{V664E} mice with 6 dpd, could be rescued
638 by the Dox-treatment switch. Although both mice at these conditions had exhibited
639 oligodendrocyte necroptosis or apoptosis (Fig. 8*D*, *H*), decreases of myelinating
640 oligodendrocytes (Figs. 3*A*, 5*A*), as well as dysmyelination (Fig. 9*B*, *C*, *I*, *J*), in the corpus
641 callosum on the day before Dox-treatment switching, they became mostly normal after 10-
642 day removal/addition of Dox. The MBP intensities and distributions returned to normal

(Fig. 9*A-C*, *H-J*). There were no necroptotic or apoptotic signals in the corpus callosum (Fig. 9*D,K*), and numbers of oligodendrocytes ($CC1^+$, $Olig2^+$) became as same as those in control mice (Fig. 9*E-G*, *L-N*), despite that proliferative OPCs in *Plp*-ErbB2^{V664E} mice had not completely returned to normal at this time (Fig. 9*E-G*). In a word, MO necroptosis and OPC apoptosis can be ceased by suppressing the aberrant activation of ErbB receptors, and the dead oligodendrocytes, irrespective of inflammatory status, can be cleaned to restore myelin development. These results suggest that the early interference with aberrant ErbB signaling is effective to prevent the white matter pathological progression.

Discussion

The results from *in vivo* pulse-labeled reporter tracing and *in vitro* transgene-expressing cell examination were consistent with the fact that the death was occurred for OPCs in *Sox10*-ErbB2^{V664E} mice but for MOs in *Plp*-ErbB2^{V664E} mice. These results substantiate that *Sox10*$^{+/rtTA}$ and *Plp*-tTA mice are valuable tools for *in vivo* exploration of molecular and cellular mechanisms that involve oligodendrocyte development and pathogenesis. In the present study, the differentiation-stage targeting preferences of *Sox10*$^{+/rtTA}$ and *Plp*-tTA mice helped manipulate ErbB activities in non-overlapping oligodendrocyte lineage cells, enabling us to distinguish the histological and cellular responses induced by activating ErbB receptors in MOs and OPC-NFOs, respectively. The levels of ErbB2 immunostaining intensities in individual OPCs from *Sox10*-ErbB2^{V664E} mice and individual MOs from *Plp*-ErbB2^{V664E} mice were comparable, suggesting that the transactivation activities of

tTA/rtTA at single cell levels induced in *Sox10*$^{+/rtTA}$ and *Plp*-tTA mice are the same (Fig. 7*D*). Moreover, when using real-time RT-PCR to examine the initiation of the transgene in *Sox10*-ErbB2^{V664E} and *Plp*-ErbB2^{V664E} white matter, ErbB2^{V664E} transcript significantly increased in both mice at the first day with Dox addition or removal, suggesting that the *Sox10*-rtTA and *Plp*-tTA have comparable response time to the drug induction. Therefore, the non-overlapping phenotypes observed in *Sox10*-ErbB2^{V664E} and *Plp*-ErbB2^{V664E} mice are attributed to the cellular targeting preferences of *Sox10*$^{+/rtTA}$ and *Plp*-tTA.

By analyzing *Plp*-ErbB2^{V664E} mice, we demonstrated that ErbB overactivation was pathogenetic in MOs through inducing MO necroptosis (Fig. 8*A*-*F*). The inflammatory necroptosis of MOs easily stimulate pathological responses and cytokine releases from glial cells, ependymal cells, endothelial cells, and even possibly infiltrated macrophages in the microenvironment (Burda and Sofroniew, 2014; Pasparakis and Vandenabeele, 2015), leading to a severe pathological complication (Figs. 1-3). Interestingly, studies on genetically modified mice that overexpressed hEGFR in oligodendrocyte lineage cells or overexpressed NRG1 in neurons did not report myelin pathogenesis (Aguirre et al., 2007; Brinkmann et al., 2008). Nevertheless, mice with overactivation of the ErbB downstream signaling in oligodendrocyte lineage cells exhibit myelin and axonal pathology. *Olig2*-Cre;Pten$^{flox/flox}$ mice that overactivate PI3K/Akt signaling in oligodendrocyte lineage cells have loosened myelin lamellae in the spinal cord at 14 weeks and axonal degeneration in the cervical spinal cord fasciculus gracilis at 62 weeks (Harrington et al., 2010). *Plp*-CreER;Mek/Mek mice, which overexpress a constitutively activated MEK, a MAPK kinase, in oligodendrocyte lineage cells with tamoxifen induction, have demyelination in the spinal cord 3 months after the induction of MAPK (Erk) overactivation (Ishii et al.,

689 2016). A dose-dependent detrimental effect is suggested to MEK given the fact that *Plp*-
690 CreER;+/Mek mice exhibit only hypermyelination but not demyelination even 8 months
691 after induction. However, it should be noted that half dose of MEK overactivation also
692 induces astrogliosis and microgliosis, two inflammatory pathological symptoms in the
693 CNS, in the spinal cord 8 months after induction (Ishii et al., 2016), indicating that
694 pathogenetic events might have been sporadically occurred in the white matter of *Plp*-
695 CreER;+/Mek mice. The rapid deterioration in the corpus callosum of *Plp*-ErbB2^{V664E} mice
696 after 9 dpd should be ascribed to significant inflammation that accelerated and aggravated
697 myelin degradation (Fig. 1*L*-*N*). In contrast, the optic nerve in *Plp*-ErbB2^{V664E} mice had
698 milder inflammatory status and thus had slow myelin degradation and axon degeneration
699 at 14 dpd (Fig. 1*K*, *N*). Mild inflammation may also explain the fact that it takes 3-12
700 months for *Olig*-cre;Pten$^{flox/flox}$ and *Plp*-creER;Mek/Mek mice to develop myelin
701 breakdown and other pathological changes in white matter (Harrington et al., 2010; Ishii
702 et al., 2016).

703 Devastating effects of ErbB2^{V664E} in *Plp*-ErbB2^{V664E} mice may be due to its potent
704 promotion of endogenous ErbB activation and multiple downstream signaling including
705 both PI-3K/Akt and MAPK (Erk) pathways (Fig. 1*D*, *E*). There may be a dose-dependent
706 effect for timing or severity of the pathological responses; however, observations in *Plp*-
707 ErbB2^{V664E}, *Olig2*-Cre;Pten$^{flox/flox}$, and *Plp*-CreER;Mek/Mek mice corroborate the concept
708 that continuously activating ErbB signaling in oligodendrocyte lineage cells is
709 pathogenetic. Given the fact that *Plp*-CreER and Olig2-Cre mice target the full
710 oligodendrocyte lineage including OPCs (Guo et al., 2009), the cellular mechanism for
711 myelin pathogenesis in the previous reports was not determined. With the advantage of

712 *Sox10*$^{+/rtTA}$ mice that mainly target OPC-NFOs, we demonstrated that overactivation of
713 ErbB receptors that mediate NRG signaling in OPCs induced apoptosis, leading to non-
714 inflammatory hypomyelination (Figs. 4, 5, 8). On the other hand, the study on *Plp*-
715 ErbB2^{V664E} mice suggested that synergistic overactivation of ErbB receptors that mediate
716 NRG (ErbB3/ErbB4) and EGF (EGFR) signaling in white matter leads to more deleterious
717 pathological changes stimulating inflammation (Figs. 1, 3, 8). The differences in *Plp*-
718 ErbB2^{V664E} and *Sox10*-ErbB2^{V664E} mice demonstrated that ErbB overactivation in MOs,
719 but not OPC-NFOs, triggers inflammatory pathogenesis.

720 The present study revealed that oligodendrocytes and OPCs are cell types susceptible
721 to cell deaths induced by ErbB overactivation, different from astrocytes that become
722 hypertrophic and proliferative with ErbB overactivation (Chen et al., 2017). Notably, it has
723 been reported that overactivation of ErbB receptors can cause cell death, although in many
724 cases ErbB signaling is demonstrated to promote cell proliferation and survival. A number
725 of studies reveal the roles of ErbB4, EGFR, ErbB2 activation in necrosis or apoptosis of
726 macrophages, cancer cells, and a variety of cell types (Hognason et al., 2001; Tikhomirov
727 and Carpenter, 2004; Jackson and Ceresa, 2017; Schumacher et al., 2017). ErbB ligand-
728 induced cell death mostly occurs to cells with high ErbB receptor expression, highlighting
729 that the excessive activation of ErbB receptors is the key to inducing death pathways.
730 Consistently, their downstream Akt and Erk signaling have also been causally linked to
731 cell deaths in some cases (Maddika et al., 2007; Wu et al., 2009; Cagnol and Chambard,
732 2010). It is intriguing that ErbB receptor overactivation in MOs and OPCs induced distinct
733 deleterious effects. Because that RIP3 and MLKL, the core components of necroptotic
734 machinery, increased specifically in MOs (Fig. 8*D*), but not in astrocytes or microglia

735 which were also pathologically activated in *Plp*-ErbB2^{V664E} white matter (Fig. 1*L*, *M*), the
736 necroptosis signaling should be activated by intracellular signaling pathways downstream
737 of ErbB receptors in MOs. Caspase-8 activation has been reported to be the key event to
738 determine apoptotic fate of cells (Oberst et al., 2011), and defective activation of caspase-
739 8 is critical for RIP1/RIP3/MLKL signaling to induce oligodendrocyte necroptosis in
740 multiple sclerosis (Ofengeim et al., 2015). A cell-type specific RNA-sequencing
741 transcriptome analysis suggests that caspase-8 is minimally expressed in post-mitotic
742 oligodendrocytes but is detectable in OPCs (Zhang et al., 2014), which may determine MO
743 necroptosis but OPC apoptosis under continuous ErbB activation.

744 The demyelinating disease is now a broad concept that embraces more than multiple
745 sclerosis, neuromyelitis optica, and leukodystrophy. Increasing evidence points to the
746 correlation of the common demyelinating diseases with psychological symptoms (Diaz-
747 Olavarrieta et al., 1999; Chiaravalloti and DeLuca, 2008). On the other hand, white matter
748 lesion is an emerging feature that can be examined periodically by structural brain imaging
749 in patients with psychiatric disorders (Fields, 2008; Mei and Nave, 2014). Remarkably,
750 elevated ErbB activation has been repeatedly implicated in schizophrenia. For example,
751 the mRNA and protein levels of NRG1 and ErbB4 are reported to increase in the prefrontal
752 cortex and hippocampus of schizophrenic patients (Law et al., 2006; Chong et al., 2008;
753 Joshi et al., 2014). These increases could be caused by genetic factors, such as
754 schizophrenia-linked single nucleotide-polymorphisms (SNPs) SNP8NRG221132 and
755 SNP8NRG243177, which are identified to increase the mRNA levels of NRG1 (Law et al.,
756 2006). In addition to increased expression, it has been shown that the capacity for ErbB4
757 to be activated is markedly improved in the prefrontal cortex of schizophrenic patients

758 (Hahn et al., 2006). Besides NRG1 and ErbB4 that have received extensive attention,
759 EGFR is observed to increase in the brain of some schizophrenic patients (Futamura et al.,
760 2002).

761 The white matter abnormalities observed in our mouse models are reminiscent of
762 diverse myelin-related clinical characteristics in schizophrenic brains, including reduced
763 white matter volume, decreased oligodendrocyte densities, reduced myelin gene products,
764 apoptotic oligodendrocytes, and damaged myelin (Douaud et al., 2007; Uranova et al.,
765 2007; Fields, 2008; Hoistad et al., 2009; Uranova et al., 2011). To our knowledge, we are
766 the first to reveal that ErbB overactivation can primarily induce oligodendropathy and
767 myelin pathogenesis in white matter, providing a possible predisposition of a genetic
768 variability in the ErbB receptors or ligands to the white matter lesion. Notably,
769 SNP8NRG243177 with T-allele, which increases NRG1 Type IV production (Law et al.,
770 2006), is associated with the reduced white matter integrity in schizophrenic patients
771 (McIntosh et al., 2008). The direct evidence provided by the present study that gain of
772 function in ErbB receptors caused primary white matter lesions emphasizes that monitoring
773 white matter in live patients and testing the genetic variability of ErbB signaling pathways
774 are two necessary methods to help develop prognostic and therapeutic strategies for
775 psychiatric disorders.

776 Intrinsic genetic alterations, apart from the pathogenetic immune responses, may also
777 cause primary oligodendropathy in multiple sclerosis (Factor et al., 2020).
778 Oligodendrocyte necroptosis has been revealed to be a hallmark in multiple sclerosis
779 (Ofengeim et al., 2015), indicating that ErbB receptor activation is possible an upstream
780 pathogenic mechanism for the most common demyelinating disease. It has been reported

781 that inhibition of MAPK (Erk) activity by PD0325901, a MEK inhibitor, promotes OPC
782 differentiation and myelin regeneration in two different animal models of the
783 demyelinating disease (Suo et al., 2019). Moreover, an EGF antibody has been used to
784 neutralize EGF in the animal model of multiple sclerosis and exhibits therapeutic effects
785 by promoting oligodendrogenesis and ameliorating pathological status (Amir-Levy et al.,
786 2014). Therefore, our findings provide a novel molecular and cellular insight into the
787 primary oligodendropathy in demyelinating diseases, and support that early intervention of
788 ErbB overactivation is beneficial in the therapy of the diseases.

789 **References**

790 Aguirre A, Dupree JL, Mangin JM, Gallo V (2007) A functional role for EGFR signaling
791 in myelination and remyelination. Nat Neurosci 10:990-1002.

792 Amir-Levy Y, Mausner-Fainberg K, Karni A (2014) Treatment with Anti-EGF Ab
793 Ameliorates Experimental Autoimmune Encephalomyelitis via Induction of
794 Neurogenesis and Oligodendrogenesis. Mult Scler Int 2014:926134.

795 Bercury KK, Dai J, Sachs HH, Ahrendsen JT, Wood TL, Macklin WB (2014) Conditional
796 ablation of raptor or rictor has differential impact on oligodendrocyte
797 differentiation and CNS myelination. J Neurosci 34:4466-4480.

798 Bergles DE, Richardson WD (2015) Oligodendrocyte Development and Plasticity. Cold
799 Spring Harb Perspect Biol 8:a020453.

800 Bradl M, Lassmann H (2010) Oligodendrocytes: biology and pathology. Acta Neuropathol
801 119:37-53.

802 Brinkmann BG, Agarwal A, Sereda MW, Garratt AN, Muller T, Wende H, Stassart RM,
803 Nawaz S, Humml C, Velanac V, Radyushkin K, Goebbels S, Fischer TM, Franklin
804 RJ, Lai C, Ehrenreich H, Birchmeier C, Schwab MH, Nave KA (2008) Neuregulin-
805 1/ErbB signaling serves distinct functions in myelination of the peripheral and
806 central nervous system. Neuron 59:581-595.

807 Burda JE, Sofroniew MV (2014) Reactive gliosis and the multicellular response to CNS
808 damage and disease. Neuron 81:229-248.

809 Cagnol S, Chambard JC (2010) ERK and cell death: mechanisms of ERK-induced cell
810 death--apoptosis, autophagy and senescence. FEBS J 277:2-21.

811 Chassin H, Muller M, Tigges M, Scheller L, Lang M, Fussenegger M (2019) A modular
812 degron library for synthetic circuits in mammalian cells. Nat Commun 10:2013.
813 Chen J, He W, Hu X, Shen Y, Cao J, Wei Z, Luan Y, He L, Jiang F, Tao Y (2017) A role
814 for ErbB signaling in the induction of reactive astrogliosis. Cell Discov 3:17044.
815 Chiaravalloti ND, DeLuca J (2008) Cognitive impairment in multiple sclerosis. Lancet
816 Neurol 7:1139-1151.
817 Chong VZ, Thompson M, Beltaifa S, Webster MJ, Law AJ, Weickert CS (2008) Elevated
818 neuregulin-1 and ErbB4 protein in the prefrontal cortex of schizophrenic patients.
819 Schizophr Res 100:270-280.
820 Corish P, Tyler-Smith C (1999) Attenuation of green fluorescent protein half-life in
821 mammalian cells. Protein Eng 12:1035-1040.
822 Czopka T, Ffrench-Constant C, Lyons DA (2013) Individual oligodendrocytes have only
823 a few hours in which to generate new myelin sheaths in vivo. Dev Cell 25:599-609.
824 Diaz-Olavarrieta C, Cummings JL, Velazquez J, Garcia de la Cadena C (1999)
825 Neuropsychiatric manifestations of multiple sclerosis. J Neuropsychiatry Clin
826 Neurosci 11:51-57.
827 Douaud G, Smith S, Jenkinson M, Behrens T, Johansen-Berg H, Vickers J, James S, Voets
828 N, Watkins K, Matthews PM, James A (2007) Anatomically related grey and white
829 matter abnormalities in adolescent-onset schizophrenia. Brain 130:2375-2386.
830 Emery B, Lu QR (2015) Transcriptional and Epigenetic Regulation of Oligodendrocyte
831 Development and Myelination in the Central Nervous System. Cold Spring Harb
832 Perspect Biol 7:a020461.

833 Factor DC et al. (2020) Cell Type-Specific Intralocus Interactions Reveal Oligodendrocyte
834 Mechanisms in MS. Cell 181:382-395 e321.
835 Fancy SP, Baranzini SE, Zhao C, Yuk DI, Irvine KA, Kaing S, Sanai N, Franklin RJ,
836 Rowitch DH (2009) Dysregulation of the Wnt pathway inhibits timely myelination
837 and remyelination in the mammalian CNS. Genes Dev 23:1571-1585.
838 Fields RD (2008) White matter in learning, cognition and psychiatric disorders. Trends
839 Neurosci 31:361-370.
840 Flores AI, Mallon BS, Matsui T, Ogawa W, Rosenzweig A, Okamoto T, Macklin WB
841 (2000) Akt-mediated survival of oligodendrocytes induced by neuregulins. The
842 Journal of neuroscience : the official journal of the Society for Neuroscience
843 20:7622-7630.
844 Flores AI, Narayanan SP, Morse EN, Shick HE, Yin X, Kidd G, Avila RL, Kirschner DA,
845 Macklin WB (2008) Constitutively active Akt induces enhanced myelination in the
846 CNS. J Neurosci 28:7174-7183.
847 Fu H, Cai J, Clevers H, Fast E, Gray S, Greenberg R, Jain MK, Ma Q, Qiu M, Rowitch
848 DH, Taylor CM, Stiles CD (2009) A genome-wide screen for spatially restricted
849 expression patterns identifies transcription factors that regulate glial development.
850 J Neurosci 29:11399-11408.
851 Futamura T, Toyooka K, Iritani S, Niizato K, Nakamura R, Tsuchiya K, Someya T, Kakita
852 A, Takahashi H, Nawa H (2002) Abnormal expression of epidermal growth factor
853 and its receptor in the forebrain and serum of schizophrenic patients. Mol
854 Psychiatry 7:673-682.

855 Guo F, Ma J, McCauley E, Bannerman P, Pleasure D (2009) Early postnatal proteolipid
856 promoter-expressing progenitors produce multilineage cells in vivo. J Neurosci
857 29:7256-7270.
858 Hahn CG, Wang HY, Cho DS, Talbot K, Gur RE, Berrettini WH, Bakshi K, Kamins J,
859 Borgmann-Winter KE, Siegel SJ, Gallop RJ, Arnold SE (2006) Altered neuregulin
860 1-erbB4 signaling contributes to NMDA receptor hypofunction in schizophrenia.
861 Nat Med 12:824-828.
862 Harrington EP, Zhao C, Fancy SP, Kaing S, Franklin RJ, Rowitch DH (2010)
863 Oligodendrocyte PTEN is required for myelin and axonal integrity, not
864 remyelination. Ann Neurol 68:703-716.
865 Hognason T, Chatterjee S, Vartanian T, Ratan RR, Ernewein KM, Habib AA (2001)
866 Epidermal growth factor receptor induced apoptosis: potentiation by inhibition of
867 Ras signaling. FEBS Lett 491:9-15.
868 Hoistad M, Segal D, Takahashi N, Sakurai T, Buxbaum JD, Hof PR (2009) Linking white
869 and grey matter in schizophrenia: oligodendrocyte and neuron pathology in the
870 prefrontal cortex. Front Neuroanat 3:9.
871 Hughes EG, Orthmann-Murphy JL, Langseth AJ, Bergles DE (2018) Myelin remodeling
872 through experience-dependent oligodendrogenesis in the adult somatosensory
873 cortex. Nat Neurosci 21:696-706.
874 Inamura N, Sugio S, Macklin WB, Tomita K, Tanaka KF, Ikenaka K (2012) Gene
875 induction in mature oligodendrocytes with a PLP-tTA mouse line. Genesis 50:424-
876 428.

877 Ishii A, Furusho M, Bansal R (2013) Sustained activation of ERK1/2 MAPK in
878 oligodendrocytes and schwann cells enhances myelin growth and stimulates
879 oligodendrocyte progenitor expansion. The Journal of neuroscience : the official
880 journal of the Society for Neuroscience 33:175-186.
881 Ishii A, Furusho M, Dupree JL, Bansal R (2016) Strength of ERK1/2 MAPK Activation
882 Determines Its Effect on Myelin and Axonal Integrity in the Adult CNS. J Neurosci
883 36:6471-6487.
884 Ishii A, Fyffe-Maricich SL, Furusho M, Miller RH, Bansal R (2012) ERK1/ERK2 MAPK
885 signaling is required to increase myelin thickness independent of oligodendrocyte
886 differentiation and initiation of myelination. J Neurosci 32:8855-8864.
887 Jackson NM, Ceresa BP (2017) EGFR-mediated apoptosis via STAT3. Exp Cell Res
888 356:93-103.
889 Joshi D, Fullerton JM, Weickert CS (2014) Elevated ErbB4 mRNA is related to interneuron
890 deficit in prefrontal cortex in schizophrenia. J Psychiatr Res 53:125-132.
891 Law AJ, Lipska BK, Weickert CS, Hyde TM, Straub RE, Hashimoto R, Harrison PJ,
892 Kleinman JE, Weinberger DR (2006) Neuregulin 1 transcripts are differentially
893 expressed in schizophrenia and regulated by 5' SNPs associated with the disease.
894 Proc Natl Acad Sci U S A 103:6747-6752.
895 Liu Y, Tao YM, Woo RS, Xiong WC, Mei L (2007) Stimulated ErbB4 internalization is
896 necessary for neuregulin signaling in neurons. Biochem Biophys Res Commun
897 354:505-510.

898 Ludwig A, Schlierf B, Schardt A, Nave KA, Wegner M (2004) Sox10-rtTA mouse line for
899 tetracycline-inducible expression of transgenes in neural crest cells and
900 oligodendrocytes. Genesis 40:171-175.
901 Maddika S, Bay GH, Kroczak TJ, Ande SR, Maddika S, Wiechec E, Gibson SB, Los M
902 (2007) Akt is transferred to the nucleus of cells treated with apoptin, and it
903 participates in apoptin-induced cell death. Cell Prolif 40:835-848.
904 Makinodan M, Rosen KM, Ito S, Corfas G (2012) A critical period for social experience-
905 dependent oligodendrocyte maturation and myelination. Science 337:1357-1360.
906 McIntosh AM, Moorhead TW, Job D, Lymer GK, Munoz Maniega S, McKirdy J,
907 Sussmann JE, Baig BJ, Bastin ME, Porteous D, Evans KL, Johnstone EC, Lawrie
908 SM, Hall J (2008) The effects of a neuregulin 1 variant on white matter density and
909 integrity. Mol Psychiatry 13:1054-1059.
910 Mei L, Nave KA (2014) Neuregulin-ERBB signaling in the nervous system and
911 neuropsychiatric diseases. Neuron 83:27-49.
912 Nave KA, Salzer JL (2006) Axonal regulation of myelination by neuregulin 1. Curr Opin
913 Neurobiol 16:492-500.
914 Oberst A, Dillon CP, Weinlich R, McCormick LL, Fitzgerald P, Pop C, Hakem R, Salvesen
915 GS, Green DR (2011) Catalytic activity of the caspase-8-FLIP(L) complex inhibits
916 RIPK3-dependent necrosis. Nature 471:363-367.
917 Ofengeim D, Ito Y, Najafov A, Zhang Y, Shan B, DeWitt JP, Ye J, Zhang X, Chang A,
918 Vakifahmetoglu-Norberg H, Geng J, Py B, Zhou W, Amin P, Berlink Lima J, Qi C,
919 Yu Q, Trapp B, Yuan J (2015) Activation of necroptosis in multiple sclerosis. Cell
920 Rep 10:1836-1849.

921 Palazuelos J, Crawford HC, Klingener M, Sun B, Karelis J, Raines EW, Aguirre A (2014)
922 TACE/ADAM17 is essential for oligodendrocyte development and CNS
923 myelination. J Neurosci 34:11884-11896.
924 Pasparakis M, Vandenabeele P (2015) Necroptosis and its role in inflammation. Nature
925 517:311-320.
926 Schmucker J, Ader M, Brockschnieder D, Brodarac A, Bartsch U, Riethmacher D (2003)
927 erbB3 is dispensable for oligodendrocyte development in vitro and in vivo. Glia
928 44:67-75.
929 Schumacher MA, Hedl M, Abraham C, Bernard JK, Lozano PR, Hsieh JJ, Almohazey D,
930 Bucar EB, Punit S, Dempsey PJ, Frey MR (2017) ErbB4 signaling stimulates pro-
931 inflammatory macrophage apoptosis and limits colonic inflammation. Cell Death
932 Dis 8:e2622.
933 Sun L, Wang H, Wang Z, He S, Chen S, Liao D, Wang L, Yan J, Liu W, Lei X, Wang X
934 (2012) Mixed lineage kinase domain-like protein mediates necrosis signaling
935 downstream of RIP3 kinase. Cell 148:213-227.
936 Suo N, Guo YE, He B, Gu H, Xie X (2019) Inhibition of MAPK/ERK pathway promotes
937 oligodendrocytes generation and recovery of demyelinating diseases. Glia 67:1320-
938 1332.
939 Tao Y, Dai P, Liu Y, Marchetto S, Xiong WC, Borg JP, Mei L (2009) Erbin regulates
940 NRG1 signaling and myelination. Proc Natl Acad Sci U S A 106:9477-9482.
941 Tao Y, Shen C, Luo S, Traore W, Marchetto S, Santoni MJ, Xu L, Wu B, Shi C, Mei J,
942 Bates R, Liu X, Zhao K, Xiong WC, Borg JP, Mei L (2014) Role of Erbin in ErbB2-
943 dependent breast tumor growth. Proc Natl Acad Sci U S A 111:E4429-4438.

944 Tikhomirov O, Carpenter G (2004) Ligand-induced, p38-dependent apoptosis in cells
945 expressing high levels of epidermal growth factor receptor and ErbB-2. J Biol
946 Chem 279:12988-12996.
947 Trapp BD, Nishiyama A, Cheng D, Macklin W (1997) Differentiation and death of
948 premyelinating oligodendrocytes in developing rodent brain. J Cell Biol 137:459-
949 468.
950 Tripathi RB, Jackiewicz M, McKenzie IA, Kougioumtzidou E, Grist M, Richardson WD
951 (2017) Remarkable Stability of Myelinating Oligodendrocytes in Mice. Cell Rep
952 21:316-323.
953 Uranova NA, Vikhreva OV, Rachmanova VI, Orlovskaya DD (2011) Ultrastructural
954 alterations of myelinated fibers and oligodendrocytes in the prefrontal cortex in
955 schizophrenia: a postmortem morphometric study. Schizophr Res Treatment
956 2011:325789.
957 Uranova NA, Vostrikov VM, Vikhreva OV, Zimina IS, Kolomeets NS, Orlovskaya DD
958 (2007) The role of oligodendrocyte pathology in schizophrenia. Int J
959 Neuropsychopharmacol 10:537-545.
960 Wachter RM, Elsliger MA, Kallio K, Hanson GT, Remington SJ (1998) Structural basis of
961 spectral shifts in the yellow-emission variants of green fluorescent protein.
962 Structure 6:1267-1277.
963 Watkins TA, Emery B, Mulinyawe S, Barres BA (2008) Distinct stages of myelination
964 regulated by gamma-secretase and astrocytes in a rapidly myelinating CNS
965 coculture system. Neuron 60:555-569.

966 Wegener A, Deboux C, Bachelin C, Frah M, Kerninon C, Seilhean D, Weider M, Wegner
967 M, Nait-Oumesmar B (2015) Gain of Olig2 function in oligodendrocyte
968 progenitors promotes remyelination. Brain 138:120-135.
969 Wu YT, Tan HL, Huang Q, Ong CN, Shen HM (2009) Activation of the PI3K-Akt-mTOR
970 signaling pathway promotes necrotic cell death via suppression of autophagy.
971 Autophagy 5:824-834.
972 Xiao L, Ohayon D, McKenzie IA, Sinclair-Wilson A, Wright JL, Fudge AD, Emery B, Li
973 H, Richardson WD (2016) Rapid production of new oligodendrocytes is required
974 in the earliest stages of motor-skill learning. Nat Neurosci 19:1210-1217.
975 Ye F, Chen Y, Hoang T, Montgomery RL, Zhao XH, Bu H, Hu T, Taketo MM, van Es JH,
976 Clevers H, Hsieh J, Bassel-Duby R, Olson EN, Lu QR (2009) HDAC1 and HDAC2
977 regulate oligodendrocyte differentiation by disrupting the beta-catenin-TCF
978 interaction. Nat Neurosci 12:829-838.
979 Ying Z, Pan C, Shao T, Liu L, Li L, Guo D, Zhang S, Yuan T, Cao R, Jiang Z, Chen S,
980 Wang F, Wang X (2018) Mixed Lineage Kinase Domain-like Protein MLKL
981 Breaks Down Myelin following Nerve Injury. Mol Cell 72:457-468 e455.
982 Zhang Y, Chen K, Sloan SA, Bennett ML, Scholze AR, O'Keeffe S, Phatnani HP, Guarnieri
983 P, Caneda C, Ruderisch N, Deng S, Liddelow SA, Zhang C, Daneman R, Maniatis
984 T, Barres BA, Wu JQ (2014) An RNA-sequencing transcriptome and splicing
985 database of glia, neurons, and vascular cells of the cerebral cortex. J Neurosci
986 34:11929-11947.
987

988 **Figure legends**

989

990 **Figure 1. ErbB overactivation in *Plp*-ErbB2^{V664E} mice induced inflammatory**
991 **demyelination.** Unless otherwise indicated, quantitative data were presented in the graphs
992 as mean ± s.e.m., and analyzed by unpaired *t* test. **A,** Dox treatment setting for indicated
993 mice and littermate controls. **B,** Real-time RT-PCR results of ErbB2 expression at
994 indicated day post Dox withdrawal (dpd). Statistical information for 1 dpd, $t_{(4)} = 6.72$, $P =$
995 0.0025; for 4 dpd, $t_{(4)} = 3.432$, $P = 0.026$. **C,** Walking speed and percentage of foot slips of
996 *Plp*-ErbB2^{V664E} mice and littermate controls at P35 with 14 dpd in the grid walking test. n
997 = 4 mice for each group. For steps per second, $t_{(6)} = 3.773$, $P = 0.0093$; for foot slip
998 percentage, $t_{(6)} = 12.31$, $P < 0.0001$. **D**, Western blotting of indicated proteins in white
999 matter isolated from *Plp*-ErbB2^{V664E} (PB) mice in comparison with that from littermate
1000 control mice (Ctrl). Activation status of each ErbB receptor or downstream signaling
1001 protein was examined by western blotting with the specific antibody against its
1002 phosphorylated form. **E,** Quantitative data of western blotting results. For EGFR, $t_{(4)} =$
1003 27.64, $P < 0.0001$; for ErbB3, $t_{(4)} = 19.98$, $P < 0.0001$; for ErbB4, $t_{(4)} = 10.06$, $P = 0.00055$;
1004 for Akt, $t_{(4)} = 8.096$, $P = 0.0013$; for Erk, $t_{(4)} = 4.353$, $P = 0.012$. **F,** LFB staining and MBP
1005 immunostaining results of coronal sections through the genu of the corpus callosum in *Plp*-
1006 ErbB2^{V664E} and control mice. Black arrows indicate the lower staining intensity of myelin
1007 stained in the corpus callosum. Statistical information for quantitative data of LFB intensity:
1008 the middle part at 9 dpd, $t_{(6)} = 6.345$, $P = 0.00072$; the lateral part at 9 dpd, $t_{(6)} = 3.914$, P
1009 $= 0.0078$; the middle part at 14 dpd, $t_{(6)} = 9.89$, $P < 0.0001$; the lateral part at 14 dpd, $t_{(6)} =$
1010 23.07, $P < 0.0001$. Statistical information for MBP intensity: Corpus callosum (CC), $t_{(4)} =$

1011 4.884, P = 0.0081; Cortex (CX), $t_{(4)}$ = 2.834, P = 0.047. Statistical information for MBP
1012 distribution: CC, $t_{(4)}$ = 14.53, P = 0.00013; CX, $t_{(4)}$ = 20.51, P < 0.0001. **G,** Western blotting
1013 results of MBP and ErbB2 in multiple brain regions (CX, cortex; CE, cerebellum; SC,
1014 spinal cord; ME, medulla) isolated from *Plp*-ErbB2^{V664E} (PB) and littermate control mice
1015 (Ctrl) at 14 dpd. GAPDH served as a loading control. Statistical information for CE, $t_{(4)}$ =
1016 6.35, P = 0.0032; for CX, $t_{(4)}$ = 9.243, P = 0.00076; for SC, $t_{(4)}$ = 4.118, P = 0.0146; for
1017 ME, $t_{(4)}$ = 3.634, P = 0.022. **H**, Representative EM images showed that myelin sheath
1018 ruptured and broke down in *Plp*-ErbB2^{V664E} mice at 14 dpd (red arrow). Note the associated
1019 nuclei (red asterisk) showed no chromatin condensation and nucleation. **I,** EM images of
1020 the corpus callosum (CC), optic nerve (ON), and prefrontal cortex (PFC) from *Plp*-
1021 ErbB2^{V664E} and littermate controls at 14 dpd. Quantitative data were shown for *g*-ratio
1022 analysis of myelinated axons detected by EM. Averaged *g*-ratio for each mouse were
1023 plotted as insets, presented as mean ± s.e.m., and analyzed by unpaired *t* test. For CC, $t_{(4)}$
1024 = 3.412, P = 0.027; for ON, $t_{(4)}$ = 3.083, P = 0.037; for PFC, $t_{(4)}$ = 7.11, P = 0.0021. The
1025 red arrow indicates the axon with myelin breakdown. **J,** The densities of myelinated axons,
1026 as well as the percentages of axons with myelin breakdown, examined by EM in different
1027 brain regions of *Plp*-ErbB2^{V664E} (PB) and littermate control mice (Ctrl) at 14 dpd were
1028 quantified. Statistical information for myelinated-axon density, in CC, $t_{(4)}$ = 2.683, P =
1029 0.046; in ON, $t_{(4)}$ = 1.818, P = 0.143. For the percentage of axons with myelin breakdown,
1030 in CC, $t_{(4)}$ = 29.32, P < 0.0001; in ON, $t_{(4)}$ = 6.108, P = 0.0036; in PFC, $t_{(4)}$ = 8.125, P =
1031 0.0012. **K,** Axons were reduced in the subcortical white matter (white arrows) of *Plp*-
1032 ErbB2^{V664E} mice at 14 dpd. Sagittal sections of *Plp*-ErbB2^{V664E} and littermate control mice
1033 were immunostained by monoclonal antibody TuJ1. Subcortical staining intensities were

1034 measured and plotted as mean ± s.e.m., and analyzed by unpaired *t* test. $t_{(4)} = 6.019$, $P =$
1035 0.0009. **L, M,** Astrocytes ($GFAP^+$) and microglia ($Iba1^+$) examined in the subcortical white
1036 matter of indicated mice by immunostaining. Cell densities in the corpus callosum were
1037 quantified, and data were presented as mean ± s.e.m., and analyzed by unpaired *t* test. In
1038 **L**, $t_{(10)} = 4.753$, $P = 0.0008$. In **M**, $t_{(4)} = 36.4$, $P < 0.0001$. **N,** Real-time RT-PCR results of
1039 GFAP and IL-1β transcripts in the corpus callosum (CC) and optic nerve (ON). *, $P < 0.05$;
1040 **, $P < 0.01$; ***, $P < 0.001$, PB *vs* Ctrl. #, $P < 0.05$, CC *vs* ON.
1041 See also Extended data Figure 1-1 and Figure 1-2.
1042
1043
1044 **Figure 2. *Plp*-ErbB2^{V664E} white matter exhibited hypermyelination prior to**
1045 **demyelination. A**, MBP immunostaining of brain slices from indicated mice. Note the
1046 myelin structure and distribution exhibited relatively more normal in the middle part of
1047 corpus callosum (inset 2') than that in the layer II/III of cortex (inset 1'), in *Plp*-ErbB2^{V664E}
1048 mice at 9 dpd. **B,** EM examination of axons in the midline of the corpus callosum (CC) and
1049 the prefrontal cortex (PFC) in *Plp*-ErbB2^{V664E} mice at 9 dpd. *g*-ratio was calculated for
1050 myelinated axons and averaged *g*-ratio were analyzed by unpaired *t* test (inset). For CC, $t_{(4)}$
1051 $= 3.226$, $P = 0.032$; for PFC, $t_{(4)} = 2.529$, $P = 0.065$. Red arrows indicate the axons with
1052 myelin breakdown. **C,** Quantitative data of MBP signal distribution in immunostaining
1053 results. Data were presented as mean ± s.e.m., and analyzed by unpaired *t* test. In middle
1054 CC, $t_{(6)} = 13.11$, $P < 0.0001$; in cortex layer II/III, $t_{(6)} = 26.31$, $P < 0.0001$. **D,** The densities
1055 of myelinated axons as well as the percentages of axons with myelin breakdown in EM
1056 analysis. Data were presented as mean ± s.e.m., and analyzed by unpaired *t* test. For

1057 myelinated-axon density in CC, $t_{(4)}$ =0.805, P = 0.466. For axons with myelin breakdown
1058 at 9 dpd examined by EM: in CC, $t_{(4)}$ = 3.567, P = 0.023; in PFC, $t_{(4)}$ = 4.146, P = 0.014.
1059
1060
1061 **Figure 3. ErbB overactivation induced oligodendrocyte degeneration but OPC**
1062 **regeneration in *Plp*-ErbB2^{V664E} mice. A,** The numbers of degenerating oligodendrocytes
1063 (represented by nuclei associated with CC1^{+} cell debris, white arrows) increased in the
1064 corpus callosum of *Plp*-ErbB2^{V664E} mice starting from 6 dpd as revealed by CC1
1065 immunostaining. The densities of remained intact CC1^{+} cells were reduced. **B,**
1066 Immunostaining results of NG2 in the corpus callosum of indicated mice at 9 dpd. **C,**
1067 Quantitative data of immunostaining results in *Plp*-ErbB2^{V664E} (PB) and control mice (Ctrl)
1068 with indicated Dox treatments were presented as mean ± s.e.m., and analyzed by unpaired
1069 t test. For CC1^{+} density: at 4 dpd, $t_{(4)}$ = 1.485, P = 0.212; for 6 dpd, $t_{(4)}$ = 5.203, P = 0.0065;
1070 for 9 dpd, $t_{(4)}$ = 20.95, P < 0.0001. For Olig2^{+} density: at 4 dpd, $t_{(6)}$ = 0.2923, P = 0.780; at
1071 6 dpd, $t_{(6)}$ = 3.16, P = 0.0196; at 9 dpd, $t_{(4)}$ = 8.563, P = 0.001. For NG2^{+} density at 9 dpd,
1072 $t_{(4)}$ = 9.912, P = 0.0006. **D,** Immunostaining results of Olig2 with Ki67 in the corpus
1073 callosum of indicated mice. Note there were non-specifically stained hemorrhagic spots
1074 (white asterisk), which is the consequence of inflammation, in the brain slices from *Plp*-
1075 ErbB2^{V664E} mice at 9 dpd. **E,** Quantitative data of Ki67^{+}Olig2^{+} cell density in *Plp*-
1076 ErbB2^{V664E} (PB) and control mice (Ctrl) with indicated Dox treatments were present as
1077 mean ± s.e.m., and analyzed by unpaired t test. At 4 dpd, $t_{(4)}$ = 1.187, P = 0.301; at 6 dpd,
1078 $t_{(4)}$ = 3.428, P = 0.027; at 9 dpd, $t_{(4)}$ = 8, P = 0.0013.
1079 See also Extended data Figure 3-1.

1080

1081

1082 **Figure 4. ErbB overactivation caused non-inflammatory hypomyelination in *Sox10*-**
1083 **ErbB2^{V664E} mice.** Unless otherwise indicated, quantitative data were presented as mean ±
1084 s.e.m., and analyzed by unpaired *t* test. **A,** Dox treatment setting for indicated mice and
1085 littermate controls. **B,** Real-time RT-PCR results of ErbB2 expression at indicated day with
1086 Dox treatment (dwd). Statistical information for 1 dpd, $t_{(10)} = 4.081$, $P = 0.0022$; for 4 dpd,
1087 $t_{(4)} = 6.37$, $P = 0.0031$. **C,** Walking speed and percentage of foot slips of *Sox10*-ErbB2^{V664E}
1088 mice and littermate controls at 9 dwd in the grid walking test. n = 4 mice for each group.
1089 Statistical information for steps per second, $t_{(6)} = 3.504$, $P = 0.0128$; for foot slip percentage,
1090 $t_{(6)} = 4.429$, $P = 0.0044$. **D,** Western blotting of indicated proteins in white matter tissues
1091 isolated from *Sox10*-ErbB2^{V664E} (SB) mice in comparison with that from littermate control
1092 mice (Ctrl). Activation status of each ErbB receptor or downstream signaling protein was
1093 examined by western blotting with the specific antibody against its phosphorylated form.
1094 **E, F,** Quantitative data of western blotting results. In **E**, statistical information for EGFR,
1095 $t_{(4)} = 0.1983$, $P = 0.852$; for ErbB3, $t_{(4)} = 28.34$, $P < 0.0001$; for ErbB4, $t_{(4)} = 9.181$, $P =$
1096 0.00078; for Akt, $t_{(4)} = 3.380$, $P = 0.028$; for Erk, $t_{(4)} = 4.899$, $P = 0.008$. In **F**, for MBP, $t_{(4)}$
1097 $= 48.82$, $P < 0.0001$. **G**, LFB staining and MBP immunostaining results of coronal sections
1098 through the genu of the corpus callosum in *Sox10*-ErbB2^{V664E} (SB) and control mice (Ctrl).
1099 Black arrows indicate the lower staining intensity of myelin stained in the corpus callosum.
1100 Statistical information for quantitative data of LFB intensity: the middle part, $t_{(6)} = 15.17$,
1101 $P < 0.0001$; the lateral part, $t_{(6)} = 10.23$, $P < 0.0001$. Statistical information for MBP
1102 intensity: CC, $t_{(8)} = 5.14$, $P = 0.0009$; CX, $t_{(4)} = 4.091$, $P = 0.015$. Statistical information

1103 for MBP distribution: CC, $t_{(8)}$ = 4.622, P = 0.0017; CX, $t_{(4)}$ = 0.997, P = 0.375. **H,** EM
1104 images of the corpus callosum (CC), optic nerve (ON), and prefrontal cortex (PFC) from
1105 *Sox10*-ErbB2^{V664E} and littermate controls at 9 dwd. Quantitative data were shown for *g*-
1106 ratio analysis of myelinated axons detected by EM. Averaged *g*-ratio for each mouse were
1107 plotted as insets, presented as mean ± s.e.m., and analyzed by unpaired *t* test. For CC, $t_{(4)}$
1108 = 3.295, P = 0.0301; for ON, $t_{(4)}$ = 3.775, P = 0.0195; for PFC, $t_{(4)}$ = 1.196, P = 0.298. **I,**
1109 The densities of myelinated axons examined by EM in different brain regions of *Sox10*-
1110 ErbB2^{V664E} (SB) and littermate control mice (Ctrl) at 9 dwd were quantified. Statistical
1111 information for CC, $t_{(4)}$ = 0.2773, P = 0.795; for ON, $t_{(4)}$ = 0.1455, P = 0.891. **J, K,**
1112 Astrocytes (GFAP^{+}) and microglia (Iba1^{+}) examined in the subcortical white matter of
1113 indicated mice by immunostaining. Cell densities in the corpus callosum were quantified,
1114 and data were presented as mean ± s.e.m., and analyzed by unpaired *t* test. In **J**, $t_{(4)}$ = 0.0501,
1115 P = 0.962. In **K**, $t_{(4)}$ = 1.637, P = 0.178. **L**, Real-time RT-PCR results of IL-1β and TNFα
1116 transcripts in the corpus callosum (CC). Data were presented as mean ± s.e.m., and
1117 statistical analysis by unpaired *t* test revealed no differences.
1118 See also Extended data Figure 4-1, Figure 1-1, and Figure 1-2.
1119
1120
1121 **Figure 5. ErbB overactivation induced oligodendrocyte number reduction in *Sox10*-**
1122 **ErbB2^{V664E} mice. A, B,** Olig2^{+}, CC1^{+}, and NG2^{+} cells in the corpus callosum of indicated
1123 mice at P27 with 6 dwd (**A**) or at P30 with 9 dwd (**B**) were examined by immunostaining.
1124 **C,** Statistic results of Olig2^{+}, CC1^{+}, and NG2^{+} cell densities in the corpus callosum of
1125 *Sox10*-ErbB2^{V664E} (SB) mice and littermate controls (Ctrl) with 6 dwd or 9 dwd. Data were

1126 from repeated immunostaining of 3 mice for each group, presented as mean ± s.e.m., and
1127 analyzed by unpaired *t* test. Statistical information for 6 dwd: Olig2$^+$, $t_{(15)}$ = 2.543, P =
1128 0.0225; CC1$^+$, $t_{(6)}$ = 3.006, P = 0.0238; PDGFRα$^+$, $t_{(13)}$ = 3.236, P = 0.0065. For 9 dwd:
1129 Olig2$^+$, $t_{(4)}$ = 6.236, P = 0.0034; CC1$^+$, $t_{(4)}$ = 16.92, P < 0.0001; NG2$^+$, $t_{(4)}$ = 3.634, P =
1130 0.0221. **D,** Immunostaining results of Olig2 with Ki67 in the corpus callosum of *Sox10*-
1131 ErbB2^{V664E} (SB) and control mice (Ctrl) at P27 with 6 dwd. Statistical information for
1132 quantitative data of Ki67$^+$Olig2$^+$ cell density: $t_{(6)}$ = 6.629, P = 0.0006.
1133 See also Extended data Figure 5-1.
1134
1135
1136 **Figure 6. *Plp*-tTA targeted MOs whereas *Sox10*$^{+/rtTA}$ targeted OPC-NFOs in mouse**
1137 **brains during postnatal development. A,** Schematic illustration of stereotaxic injection
1138 sites of AAV-*TRE*-YFP. **B, C,** Percentage of Olig2$^+$YFP$^+$, CC1$^+$YFP$^+$, or PDGFRα$^+$YFP$^+$
1139 (NG2$^+$YFP$^+$) cells in YFP$^+$ cells for *Plp*-tTA or *Sox10*$^{+/rtTA}$ mice 1 (AAV-1d) or 2 days
1140 (AAV-2d) after AAV-*TRE*-YFP injection at P14 (**B**) or P35 (**C**). Data were from repeated
1141 immunostaining results of 3-7 mice for each group, presented as mean ± s.e.m., and
1142 analyzed by unpaired *t* test. For *Plp*-tTA at P14 from AAV-1d to AAV-2d: Olig2$^+$YFP$^+$
1143 cells, $t_{(12)}$ = 0.3698, P = 0.718; CC1$^+$YFP$^+$ cells, $t_{(13)}$ = 0.5666, P = 0.581; PDGFRα$^+$YFP$^+$
1144 cells, $t_{(10)}$ = 7.532, P < 0.0001. For *Sox10*-rtTA at P14 from AAV-1d to AAV-2d:
1145 Olig2$^+$YFP$^+$ cells, $t_{(13)}$ = 0.2055, P = 0.840; CC1$^+$YFP$^+$ cells, $t_{(8)}$ = 0.6425, P = 0.539;
1146 PDGFRα$^+$YFP$^+$ cells, $t_{(5)}$ = 1.021, P = 0.354. For *Plp*-tTA at P35 from AAV-1d to AAV-
1147 2d: Olig2$^+$YFP$^+$ cells, $t_{(17)}$ = 0.4959, P = 0.626; CC1$^+$YFP$^+$ cells, $t_{(9)}$ = 2.32, P = 0.046;
1148 NG2$^+$YFP$^+$ cells, $t_{(18)}$ = 1.003, P = 0.329. For *Sox10*-rtTA at P35 from AAV-1d to AAV-

1149 2d: Olig2^{+}YFP^{+} cells, $t_{(11)} = 1.098$, $P = 0.296$; CC1^{+}YFP^{+} cells, $t_{(23)} = 0.8614$, $P = 0.398$;
1150 NG2^{+}YFP^{+} cells, $t_{(26)} = 7.869$, $P < 0.0001$. **D,** Immunostaining revealed that TCF4 was
1151 specifically expressed in a small fraction of Olig2^{+} cells, but not in PDGFRα^{+} cells, in the
1152 corpus callosum of mice at P30. Solid arrow, representative double positive cell; Open
1153 arrow, representative cell positive for TCF4 only. **E, F,** Double immunostaining results of
1154 TCF4 and YFP for brain slices from indicated mice 1 (AAV-1d) or 2 days (AAV-2d) after
1155 virus injection at P14 (**E**) or P35 (**F**). Note that TCF4^{+} nuclei in AAV-infected area were
1156 almost all localized in YFP^{+} cells in *Sox10*$^{+/rtTA}$ mice 1 day after virus injection (AAV-1d)
1157 at either P14 or P35, and the colocalization reduced after 1 more day (AAV-2d). Solid
1158 arrows, representative double positive cells; Open arrows, representative cells positive for
1159 TCF4 only. **G, H,** The percentage of TCF4^{+}YFP^{+} in YFP^{+} cells (**G**), and the density of
1160 TCF4^{+}YFP^{+} cells (**H**), were analyzed. Data were from repeated immunostaining results of
1161 3-7 mice for each group, presented as mean ± s.e.m., and analyzed by unpaired *t* test. For
1162 the percentage in *Plp*-tTA mice from AAV-1d to AAV-2d: at P14, $t_{(26)} = 1.574$, $P = 0.128$;
1163 at P35, $t_{(22)} = 2.367$, $P = 0.027$. For the percentage in *Sox10*$^{+/rtTA}$ mice from AAV-1d to
1164 AAV-2d: at P14, $t_{(10)} = 4.39$, $P = 0.0014$; at P35, $t_{(28)} = 6.041$, $P < 0.0001$. For the density
1165 in *Plp*-tTA mice from AAV-1d to AAV-2d: at P14, $t_{(26)} = 1.581$, $P = 0.126$; at P35, $t_{(22)} =$
1166 1.429, $P = 0.167$. For the density in *Sox10*$^{+/rtTA}$ mice from AAV-1d to AAV-2d: at P14, $t_{(10)}$
1167 $= 5.685$, $P = 0.0002$; at P35, $t_{(28)} = 4.813$, $P < 0.0001$.
1168 See also Extended data Figure 6-1.
1169
1170

Figure 7. ErbB2^{V664E} mainly expressed in OPC-NFO stages from *Sox10*-ErbB2^{V664E} mice whereas in MOs from *Plp*-ErbB2^{V664E} mice. A, E, *In vitro* differentiation and Dox induction protocols for OPCs from *Sox10*-ErbB2^{V664E} (**A**) or *Plp*-ErbB2^{V664E} mice (**E**). DIV, day in vitro. **B, F,** Representative immunostaining images of ErbB2 with protein markers for different oligodendrocyte stages for cultured OPCs from indicated mice with illustrated differentiation and Dox treatment protocols in **A** or **E**. Open white arrows, ErbB2^{+} cells without MBP signals; Solid white arrows, oligodendrocytes with low MBP levels; Solid pink arrows, oligodendrocytes with high MBP levels. **C,** The percentages of ErbB2^{+} cells at different oligodendrocyte stages in total ErbB2^{+} cells detected in each batch staining for cultures from *Sox10*-ErbB2^{V664E} (SB) mice. Note the proportion of oligodendrocytes at each differentiation stage *in vitro* is not the same as that *in vivo*, and 'Tet-on' was not switched on for all oligodendrocytes in cultures with Dox supplementation 24 h after cell plating. **D,** The immunostaining intensities of ErbB2 in *Sox10*-ErbB2^{V664E} (SB) oligodendrocytes at each differentiation stage, as well as that in MBP^{+} *Plp*-ErbB2^{V664E} (PB) oligodendrocytes. A.U., absolute unit. **G,** The percentages of ErbB2^{+} cells at different oligodendrocyte stages in total ErbB2^{+} cells detected in each batch staining for cultures from *Plp*-ErbB2^{V664E} (PB) mice, as well as the percentages of ErbB2^{+} oligodendrocytes in total oligodendrocytes at each differentiation stage. 'Tet-off' was switched on for all oligodendrocytes in cultures from PB mice, although the proportion of oligodendrocytes at each differentiation stage *in vitro* is not the same as that *in vivo*. **H,** Schematic summary of oligodendrocyte stage-targeting preferences of *Plp*-tTA and *Sox10*$^{+/rtTA}$.

1194

1195 **Figure 8. ErbB overactivation induced MO necroptosis in *Plp*-ErbB2^{V664E} mice but**
1196 **OPC apoptosis in *Sox10*-ErbB2^{V664E} mice. A, G,** Dox treatment setting for indicated
1197 mice and littermate controls. **B, H,** Apoptotic cells (arrows) in the corpus callosum of *Plp*-
1198 ErbB2^{V664E} and control mice at 9 dpd (**B**), or *Sox10*-ErbB2^{V664E} and control mice at 6 or 9
1199 dwd (**H**), were examined by TUNEL assays and immunostaining for cleaved caspase-3.
1200 Note the increased numbers of nuclei (DAPI^{+}) and non-specifically stained hemorrhagic
1201 spots (asterisk) in the brain slice of *Plp*-ErbB2^{V664E} mice (**B**). **C,** Quantitative data of
1202 apoptotic cell densities in indicated mice. PB, *Plp*-ErbB2^{V664E}. SB, *Sox10*-ErbB2^{V664E}. Ctrl,
1203 control mice. Data were presented as mean ± s.e.m., and analyzed by unpaired *t* test. For
1204 TUNEL assay: PB, $t_{(6)} = 0.1128$, $P = 0.914$; SB, $t_{(5)} = 8.344$, $P = 0.0004$. For Caspase-3:
1205 PB, $t_{(7)} = 0.3959$, $P = 0.704$; SB, $t_{(11)} = 3.893$, $P = 0.0025$. **D, J,** Co-immunostaining results
1206 of MLKL or RIP3 with CC1 in the corpus callosum of indicated mice with indicated Dox
1207 treatments. **E,** Western blotting results of MLKL and RIP3 in the white matter of *Plp*-
1208 ErbB2^{V664E} (PB) mice, or in that of *Sox10*-ErbB2^{V664E} (SB) mice, and in those of littermate
1209 control mice (Ctrl). ns, non-specific bands. **F,** Quantitative data of immunostaining and
1210 western blotting results of MLKL or RIP3 in indicated mice at 9 days with Dox treatments.
1211 Data were presented as mean ± s.e.m., and analyzed by unpaired *t* test. In western blotting
1212 results, for RIP3 protein in PB, $t_{(4)} = 3.579$, $P = 0.023$; for MLKL protein in PB, $t_{(4)} = 13.69$,
1213 $P = 0.00017$. In immunostaining results, for percentage of RIP3^{+} in CC1^{+} cells in PB, $t_{(4)}$
1214 $= 6.002$, $P = 0.0039$; for percentage of MLKL^{+} in CC1^{+} cells in PB, $t_{(4)} = 8.202$, $P = 0.0012$.
1215 **I,** Apoptotic cells (TUNEL^{+} or cleaved caspase-3^{+}) were OPCs (NG2^{+} or PDGFRα^{+}) in
1216 *Sox10*-ErbB2^{V664E} mice at P30 with 9 dwd. Arrows, representative double positive cells.

1217 Note OPCs in *Sox10*-ErbB2^{V664E} mice were hypertrophic. The percentage of apoptotic
1218 OPCs in total OPCs were quantified and data were presented as mean ± s.e.m. and analyzed
1219 by unpaired *t* test. For TUNEL^{+}NG2^{+} cells, $t_{(4)} = 3.95$, $P = 0.0168$. For Caspase3^{+}PDGFRα^{+}
1220 cells, $t_{(4)} = 26.96$, $P < 0.0001$.
1221
1222
1223 **Figure 9. Early intervention rescued pathological phenotypes in both *Plp*-ErbB2^{V664E}**
1224 **and *Sox10*-ErbB2^{V664E} mice.** Unless otherwise indicated, quantitative data were presented
1225 as mean ± s.e.m., and analyzed by unpaired *t* test. **A, H,** Dox treatment setting for *Plp*-
1226 ErbB2^{V664E} (PB) or *Sox10*-ErbB2^{V664E} (SB) mice and littermate controls (Ctrl). **B, I,** MBP
1227 immunostaining of indicated mice with indicated Dox treatments. **C, J,** Quantitative data
1228 of MBP immunostaining results. Statistical information for PB at P27 (6 dpd) in **C**: MBP
1229 distribution of the corpus callosum (CC), $t_{(10)} = 0.6433$, $P = 0.534$; the cortex (CX), $t_{(10)} =$
1230 16.67, $P < 0.0001$. MBP intensity of CC, $t_{(10)} = 4.72$, $P = 0.0008$; CX, $t_{(10)} = 11.01$, $P < 0.0001$.
1231 For PB at P37 (6 dpd-10 dwd) in **C**: MBP distribution of CC, $t_{(10)} = 0.7256$, $P = 0.485$; CX,
1232 $t_{(10)} = 0.9144$, $P = 0.382$. MBP intensity of CC, $t_{(10)} = 0.8559$, $P = 0.412$; CX, $t_{(10)} = 0.09778$,
1233 $P = 0.924$. For the corpus callosum of SB in **J**: MBP distribution at P27 (6 dwd), $t_{(7)} = 2.93$,
1234 $P = 0.022$; at P37 (6 dwd-10 dpd), $t_{(7)} = 1.979$, $P = 0.088$. MBP intensity at P27 (6 dwd), $t_{(7)}$
1235 $= 4.478$, $P = 0.0029$; at P37 (6 dwd-10 dpd), $t_{(8)} = 1.975$, $P = 0.084$. **D, K,** No necroptotic
1236 (MLKL^{+}) or apoptotic signals (cleaved caspase-3^{+}) in *Plp*-ErbB2^{V664E} (**D**) and *Sox10*-
1237 ErbB2^{V664E} (**K**) mice, respectively, 10 days after Dox treatment switch. **E, F, L, M,**
1238 Representative immunostaining results of CC1, PDGFRα, Olig2, Ki67 in the corpus
1239 callosum of *Plp*-ErbB2^{V664E} (**E, F**) and *Sox10*-ErbB2^{V664E} (**L, M**) mice 10 days after Dox

1240 treatment switch. **G, N,** Quantitative data of oligodendrocyte densities in the corpus
1241 callosum. Statistical information for *Plp*-ErbB2^{V664E} (PB) in **G**: for CC1^{+}, $t_{(6)} = 1.288$, $P =$
1242 0.245; for Olig2^{+}, $t_{(6)} = 0.7953$, $P = 0.457$; for PDGFRα^{+}, $t_{(6)} = 3.907$, $P = 0.0079$; for
1243 Ki67^{+}Olig2^{+}, $t_{(6)} = 3.389$, $P = 0.0147$. For *Sox10*-ErbB2^{V664E} (SB) in **N**: for CC1^{+}, $t_{(6)} =$
1244 0.1294, $P = 0.901$; for Olig2^{+}, $t_{(6)} = 0.6954$, $P = 0.513$; for PDGFRα^{+}, $t_{(6)} = 0.9395$, $P =$
1245 0.384; for Ki67^{+}Olig2^{+}, $t_{(6)} = 0.5167$, $P = 0.624$.
1246
1247
1248
1249

1250 **Extended data Figure legends**

1251

1252 **Extended data Figure 1-1. No leak in transgene expression in mice at P21 before drug**
1253 **induction. A**, **D**, Western blotting of indicated proteins in white matter isolated from *Plp*-
1254 ErbB2^{V664E} (PB) mice and littermate control mice (Ctrl) at P21 before Dox withdrawal (**A**),
1255 or from *Sox10*-ErbB2^{V664E} (SB) mice and littermate control mice (Ctrl) at P21 before Dox
1256 treatment (**D**). ns, non-specific bands. **B**, **C**, **E**, **F**, Astrocytes (GFAP^{+}) and microglia (Iba1^{+})
1257 examined in the corpus callsoum of indicated mice by immunostaining. Cell densities in
1258 the corpus callosum were quantified, and data were presented as mean ± s.e.m.. Statistical
1259 analyses by unpaired *t* test revealed no differences.

1260

1261

1262 **Extended data Figure 1-2. Unaltered myelin in the brains of *Plp*-tTA or *Sox10*$^{+/rtTA}$**
1263 **mice after Dox treatments. A, B,** EM images of the corpus callosum of *Plp*-tTA and
1264 littermate *TRE*-ErbB2^{V664E} mice at P35 with 14 dpd (**A**), or that of *Sox10*$^{+/rtTA}$ and littermate
1265 *TRE*-ErbB2^{V664E} mice at P30 with 9 dwd (**B**). *g*-ratio was calculated for myelinated axons.
1266 Averaged *g*-ratio (inset) were presented as mean ± s.e.m., and analyzed by unpaired *t* test.
1267 For A, $t_{(4)} = 0.4472$, $P = 0.678$; for B, $t_{(4)} = 0.3042$, $P = 0.776$.

1268

1269

1270 **Extended data Figure 3-1. ErbB overactvation induced pathological changes in white**
1271 **matter of adult *Plp*-ErbB2^{V664E} mice. A,** Dox treatment setting for indicated mice and
1272 littermate controls. **B,** MBP immunostaining of *Plp*-ErbB2^{V664E} mice and littermate

1273 controls at P70 with 10 dpd. Magnified regions exhibited that myelin structures were
1274 comparable in the corpus callosum (CC, 1 and 1') whereas became fragmented and beaded
1275 in layer II/III of the cortex (II/III, 2 and 2') in *Plp*-ErbB2^{V664E} mice. Note there were more
1276 non-specifically stained hemorrhagic spots (white asterisk) in the cortex of these mice than
1277 that of *Plp*-ErbB2^{V664E} mice with similar treatment at P30 with 9 dpd. Quantitative data
1278 were presented as mean ± s.e.m., and analyzed by unpaired *t* test. For MBP intensity of CC,
1279 $t_{(4)} = 3.033$, $P = 0.0386$; CX-II/III, $t_{(4)} = 1.204$, $P = 0.295$. For MBP distribution of CC, $t_{(4)}$
1280 $= 0.5432$, $P = 0.616$; CX-II/III, $t_{(4)} = 67.58$, $P < 0.0001$. **C, D,** Representative
1281 immunostaining results of MLKL, CC1, PDGFRα, Olig2 in the corpus callosum of *Plp*-
1282 ErbB2^{V664E} and littermate control mice at P70 with 10 dpd. **E,** Quantitative data of
1283 oligodendrocyte densities in the corpus callosum were presented as mean ± s.e.m., and
1284 analyzed by unpaired *t* test. For MLKL$^+$, $t_{(6)} = 7.716$, $P = 0.0002$; for CC1$^+$, $t_{(6)} = 31.34$, P
1285 < 0.0001; for Olig2$^+$, $t_{(4)} = 6.372$, $P = 0.0031$; for PDGFRα$^+$, $t_{(4)} = 2.8$, $P = 0.0488$. **F**, **G**,
1286 Astrocytes (GFAP$^+$) and microglia (Iba1$^+$) examined in the subcortical white matter of
1287 indicated mice by immunostaining. **H**. Astrocyte and microglia densities in the corpus
1288 callosum were quantified, and data were presented as mean ± s.e.m., and analyzed by
1289 unpaired *t* test. For GFAP$^+$, $t_{(6)} = 3.148$, $P = 0.0199$; for Iba1$^+$, $t_{(5)} = 11.36$, $P < 0.0001$.
1290 Note the GFAP$^+$ cell densities were not increased, despite that of Iba1$^+$ cells increased
1291 dramatically, indicating a different inflammatory profile in adult mice.
1292
1293
1294 **Extended data Figure 4-1. ErbB overactvation induced hypomyelination of**
1295 **peripheral nerves in *Sox10*-ErbB2^{V664E} mice but not in *Plp*-ErbB2^{V664E} mice. A, E,**

Dox treatment setting for indicated mice and littermate controls. SCs, Schwann cells. **B**, **F**, Representative EM images of sciatic nerves for *Plp*-ErbB2^{V664E} with littermate controls (**B**), or *Sox10*-ErbB2^{V664E} with littermate controls (**F**). The top layers of EM images showed myelinated axons in the sciatic nerves, while the bottom layers of EM images showed unmyelinated axons. **C, G,** Quantitative data were shown for *g*-ratio analysis of myelinated axons detected by EM. Averaged *g*-ratio for each mouse were plotted at the bottom, presented as mean ± s.e.m., and analyzed by unpaired *t* test. For **C**, $t_{(4)} = 1.026$, $P = 0.363$; for **G**, $t_{(4)} = 12.63$, $P = 0.0002$. **D, H,** Both *Plp*-ErbB2^{V664E} and *Sox10*-ErbB2^{V664E} mice exhibited slight deficiency in unmyelinated axons of the sciatic nerves. Top: Axonal sizes of unmyelinated axons were measured by their areas in cross sections, and data were plotted as boxes showing quartile and median with whiskers to show 2.5-97.5% of data range. Outlier symbols were omitted. Data were analyzed by unpaired *t* test. Bottom: For the ensheathment analysis of unmyelinated axons, axon numbers in each pocket were counted and quantified by their frequency. For normal mature peripheral nerves, the majority of non-myelinating SC pockets only ensheathe one axon.

Extended data Figure 5-1. Oligodendrocyte cell densities were similar in the corpus callosum of *Sox10*$^{+/rtTA}$ and littermate *TRE*-ErbB2^{V664E} mice. (**A**) Olig2^{+}, CC1^{+}, and NG2^{+} cells in the corpus callosum of indicated mice at P30 with 9 dwd were examined by immunostaining. (**B**) Data were from immunostaining of 3 mice for each group, presented as mean ± s.e.m., and analyzed by unpaired *t* test. For Olig2^{+}, $t_{(4)} = 1.418$, $P = 0.229$; for CC1^{+}, $t_{(7)} = 0.3431$, $P = 0.742$; for NG2^{+}, $t_{(4)} = 1.394$, $P = 0.236$.

1319

1320

1321 **Extended data Figure 6-1. Pulse-labeled reporter-containing oligodendrocytes in *Plp*-**

1322 **tTA and *Sox10*$^{+/rtTA}$ at P14 or P35. A-D,** AAV-*TRE*-YFP was stereotactically injected

1323 into the corpus callosum of *Sox10*$^{+/rtTA}$ or *Plp*-tTA mice at P14 or P35. 1 (AAV-1d) or 2

1324 (AAV-2d) days after virus injection, brain sections were co-immunostained by antibodies

1325 to YFP and Olig2, or by CC1 antibody and antibody to YFP, or by antibodies to YFP and

1326 NG2 (or PDGFRα). Shown are representative images for indicated mice at P14 or P35.

1327 *Sox10*$^{+/rtTA}$ mice were fed with Dox for 3 days before stereotaxic injection of the virus,

1328 while *Plp*-tTA mice had no Dox treatment. **E, F,** Distributions of viral pulse-labeled cells,

1329 as shown by co-immunostaining of YFP and TCF4, in the corpus callosum of *Sox10*$^{+/rtTA}$

1330 (**E**) or *Plp*-tTA (**F**) mice at P35. Note that reporter-containing (YFP^{+}) cells in *Sox10*$^{+/rtTA}$

1331 mice stringently distributed within TCF4^{+} cell clustered region, whereas those in *Plp*-tTA

1332 mice distributed broadly in the corpus callosum. Solid arrows, regions with clustered

1333 TCF4^{+} cells; Open arrows, regions with fewer TCF4^{+} cells.

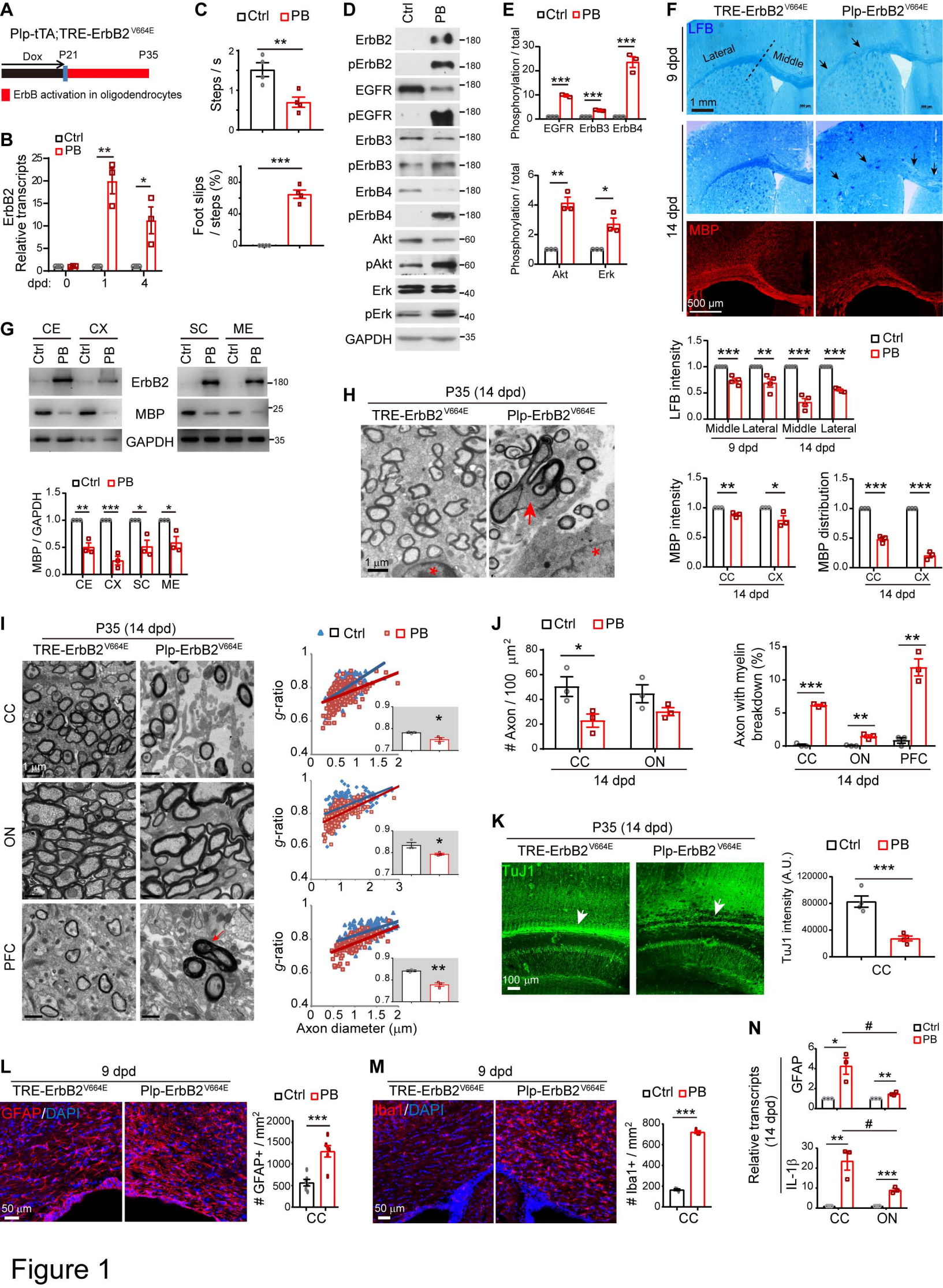
A
Plp-tTA;TRE-ErbB2V664E
Dox
P21
P35
ErbB activation in oligodendrocytes
B
Ctrl
PB
ErbB2 Relative transcripts
dpd: 0 1 4
C
Steps / s
Foot slips / steps (%)
D
Ctrl
PB
ErbB2
pErbB2
EGFR
pEGFR
ErbB3
pErbB3
ErbB4
pErbB4
Akt
pAkt
Erk
pErk
GAPDH
E
Phosphorylation / total
EGFR ErbB3 ErbB4
Akt Erk
F
TRE-ErbB2V664E
Plp-ErbB2V664E
LFB
Lateral
Middle
9 dpd
14 dpd
1 mm
MBP
500 µm
LFB intensity
Middle Lateral Middle Lateral
9 dpd 14 dpd
MBP intensity
MBP distribution
CC CX
14 dpd
G
CE CX SC ME
Ctrl PB
ErbB2
MBP
GAPDH
MBP / GAPDH
H
P35 (14 dpd)
TRE-ErbB2V664E
Plp-ErbB2V664E
1 µm
I
P35 (14 dpd)
TRE-ErbB2V664E
Plp-ErbB2V664E
CC
ON
PFC
1 µm
g-ratio
Axon diameter (µm)
J
Axon / 100 µm2
CC ON
14 dpd
Axon with myelin breakdown (%)
CC ON PFC
14 dpd
K
P35 (14 dpd)
TRE-ErbB2V664E
Plp-ErbB2V664E
TuJ1
100 µm
TuJ1 intensity (A.U.)
CC
L
9 dpd
TRE-ErbB2V664E
Plp-ErbB2V664E
GFAP/DAPI
50 µm
GFAP+ / mm2
CC
M
9 dpd
TRE-ErbB2V664E
Plp-ErbB2V664E
Iba1/DAPI
50 µm
Iba1+ / mm2
CC
N
Relative transcripts (14 dpd)
GFAP
IL-1β
CC ON

Figure 1

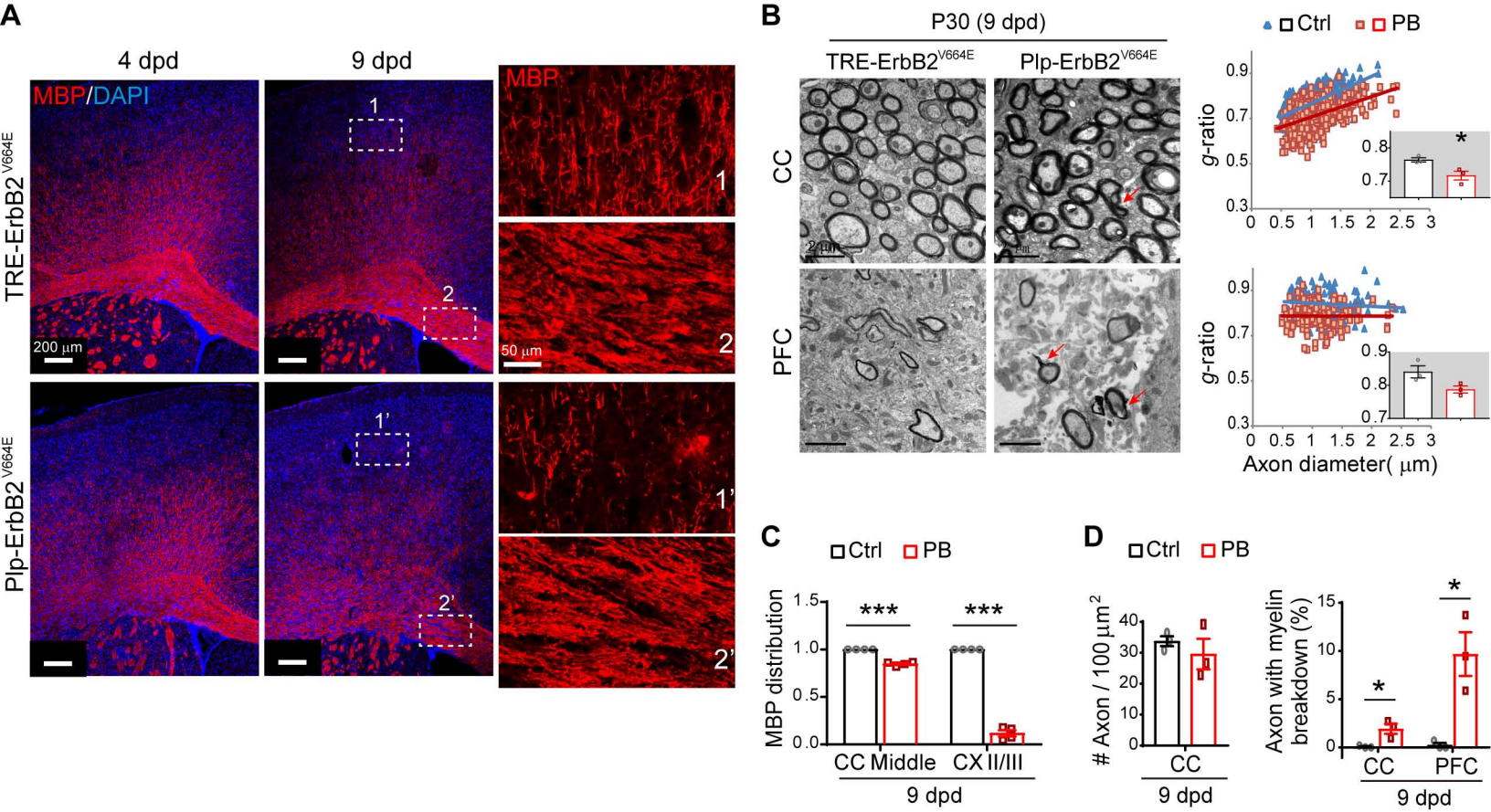
A
4 dpd
9 dpd
MBP/DAPI
MBP
TRE-ErbB2V664E
Plp-ErbB2V664E
200 µm
50 µm
1
2
1'
2'
B
P30 (9 dpd)
TRE-ErbB2V664E
Plp-ErbB2V664E
CC
PFC
Ctrl
PB
g-ratio
Axon diameter(µm)
C
Ctrl
PB
MBP distribution
***
CC Middle
CX II/III
9 dpd
D
Ctrl
PB
Axon / 100 µm2
CC
9 dpd
Axon with myelin breakdown (%)
*
CC
PFC
9 dpd

Figure 2

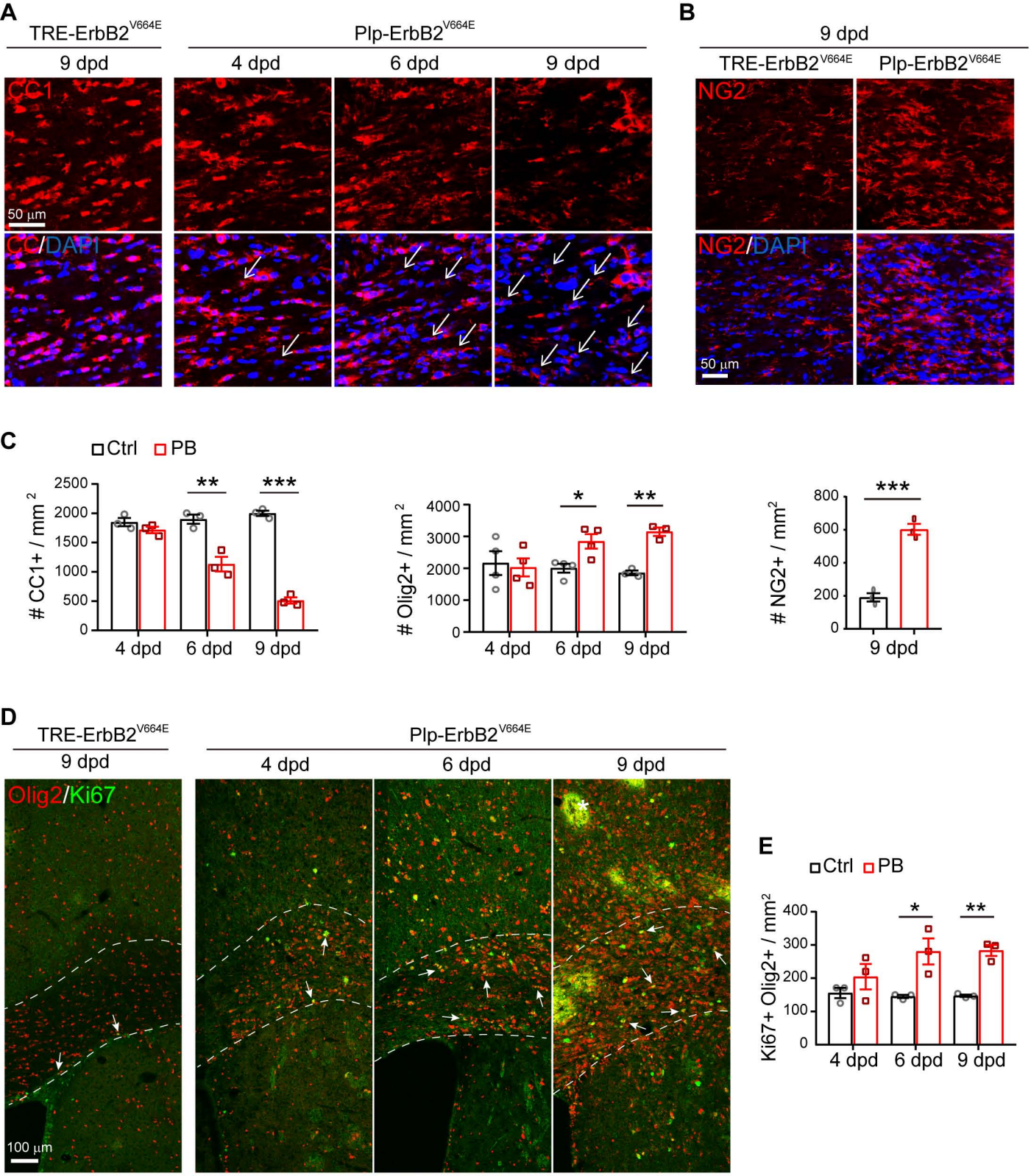
A
TRE-ErbB2V664E
Plp-ErbB2V664E
9 dpd
4 dpd
6 dpd
9 dpd
CC1
CC/DAPI
50 µm
B
9 dpd
TRE-ErbB2V664E
Plp-ErbB2V664E
NG2
NG2/DAPI
50 µm
C
Ctrl
PB
CC1+ / mm 2
Olig2+ / mm 2
NG2+ / mm2
4 dpd
6 dpd
9 dpd
D
TRE-ErbB2V664E
Plp-ErbB2V664E
9 dpd
4 dpd
6 dpd
9 dpd
Olig2/Ki67
100 µm
E
Ctrl
PB
Ki67+ Olig2+ / mm2
4 dpd
6 dpd
9 dpd

Figure 3

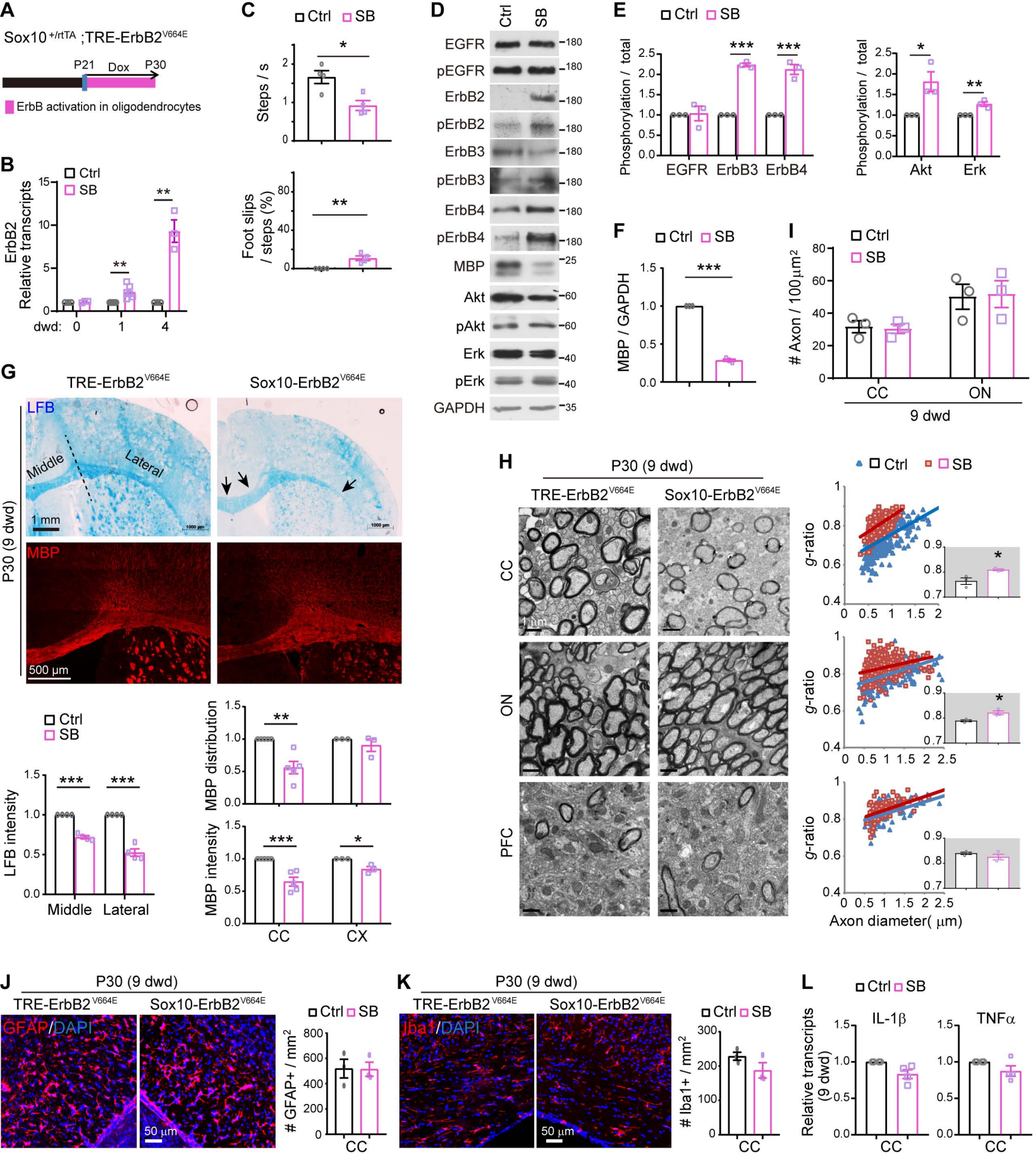
A
Sox10+/rtTA ;TRE-ErbB2V664E
P21
Dox
P30
ErbB activation in oligodendrocytes
B
Ctrl
SB
ErbB2 Relative transcripts
dwd: 0 1 4
C
Steps / s
Foot slips / steps (%)
D
Ctrl
SB
EGFR
pEGFR
ErbB2
pErbB2
ErbB3
pErbB3
ErbB4
pErbB4
MBP
Akt
pAkt
Erk
pErk
GAPDH
E
Phosphorylation / total
EGFR
ErbB3
ErbB4
Akt
Erk
F
MBP / GAPDH
I
Axon / 100μm2
CC
ON
9 dwd
G
TRE-ErbB2V664E
Sox10-ErbB2V664E
LFB
Middle
Lateral
1 mm
MBP
500 μm
P30 (9 dwd)
LFB intensity
MBP distribution
MBP intensity
CC
CX
H
P30 (9 dwd)
TRE-ErbB2V664E
Sox10-ErbB2V664E
CC
ON
PFC
1 μm
g-ratio
Axon diameter(μm)
J
P30 (9 dwd)
TRE-ErbB2V664E
Sox10-ErbB2V664E
GFAP/DAPI
50 μm
GFAP+ / mm2
K
P30 (9 dwd)
TRE-ErbB2V664E
Sox10-ErbB2V664E
Iba1/DAPI
50 μm
Iba1+ / mm2
L
IL-1β
TNFα
Relative transcripts (9 dwd)

Figure 4

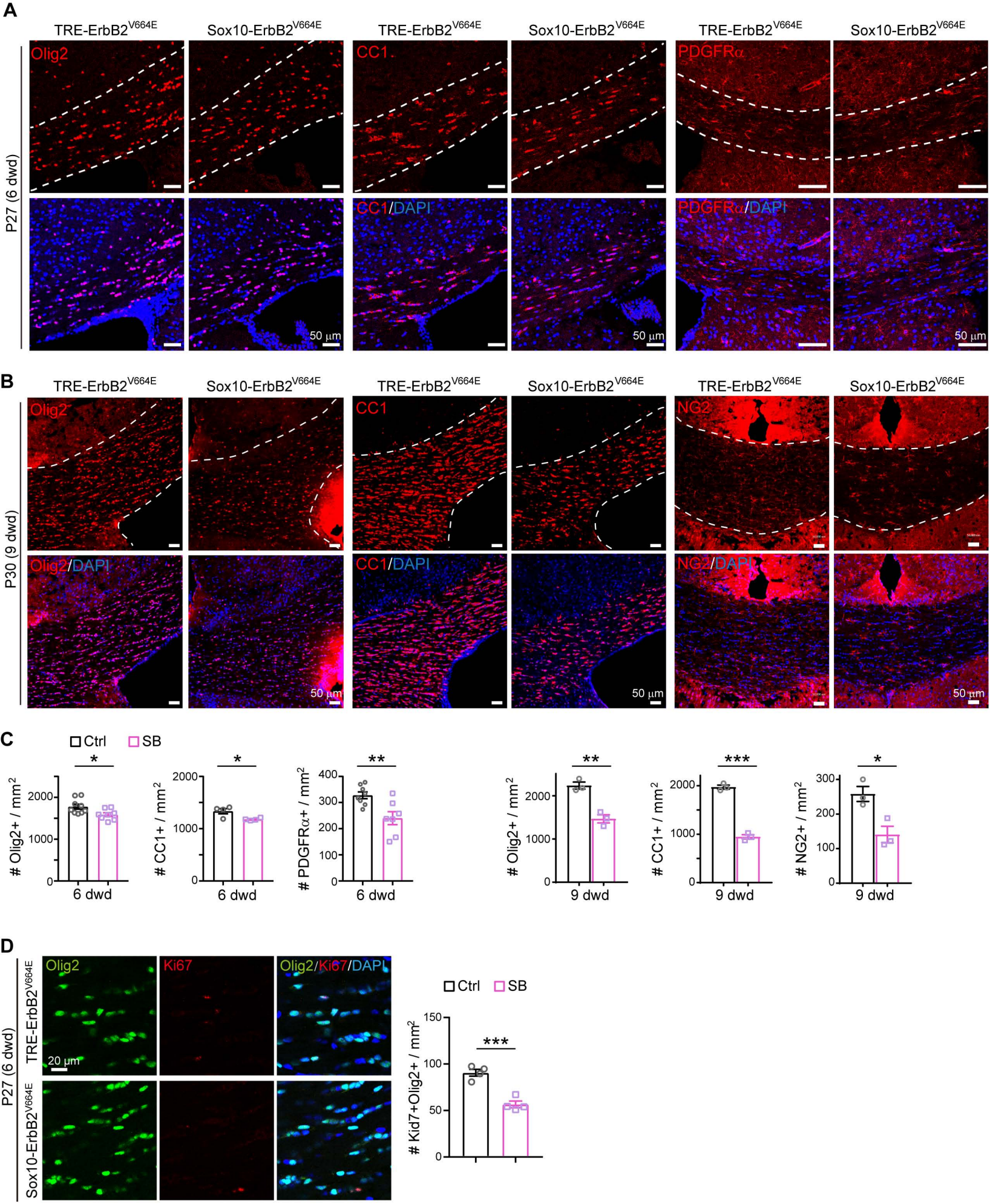
A
TRE-ErbB2V664E
Sox10-ErbB2V664E
TRE-ErbB2V664E
Sox10-ErbB2V664E
TRE-ErbB2V664E
Sox10-ErbB2V664E
P27 (6 dwd)
Olig2
CC1
PDGFRα
CC1/DAPI
PDGFRα/DAPI
50 µm
B
TRE-ErbB2V664E
Sox10-ErbB2V664E
TRE-ErbB2V664E
Sox10-ErbB2V664E
TRE-ErbB2V664E
Sox10-ErbB2V664E
P30 (9 dwd)
Olig2
CC1
NG2
Olig2/DAPI
CC1/DAPI
NG2/DAPI
50 µm
C
Ctrl
SB
Olig2+ / mm2
CC1+ / mm2
PDGFRα+ / mm2
Olig2+ / mm2
CC1+ / mm2
NG2+ / mm2
6 dwd
9 dwd
D
P27 (6 dwd)
TRE-ErbB2V664E
Sox10-ErbB2V664E
Olig2
Ki67
Olig2/Ki67/DAPI
20 µm
Ctrl
SB
Kid7+Olig2+ / mm2

Figure 5

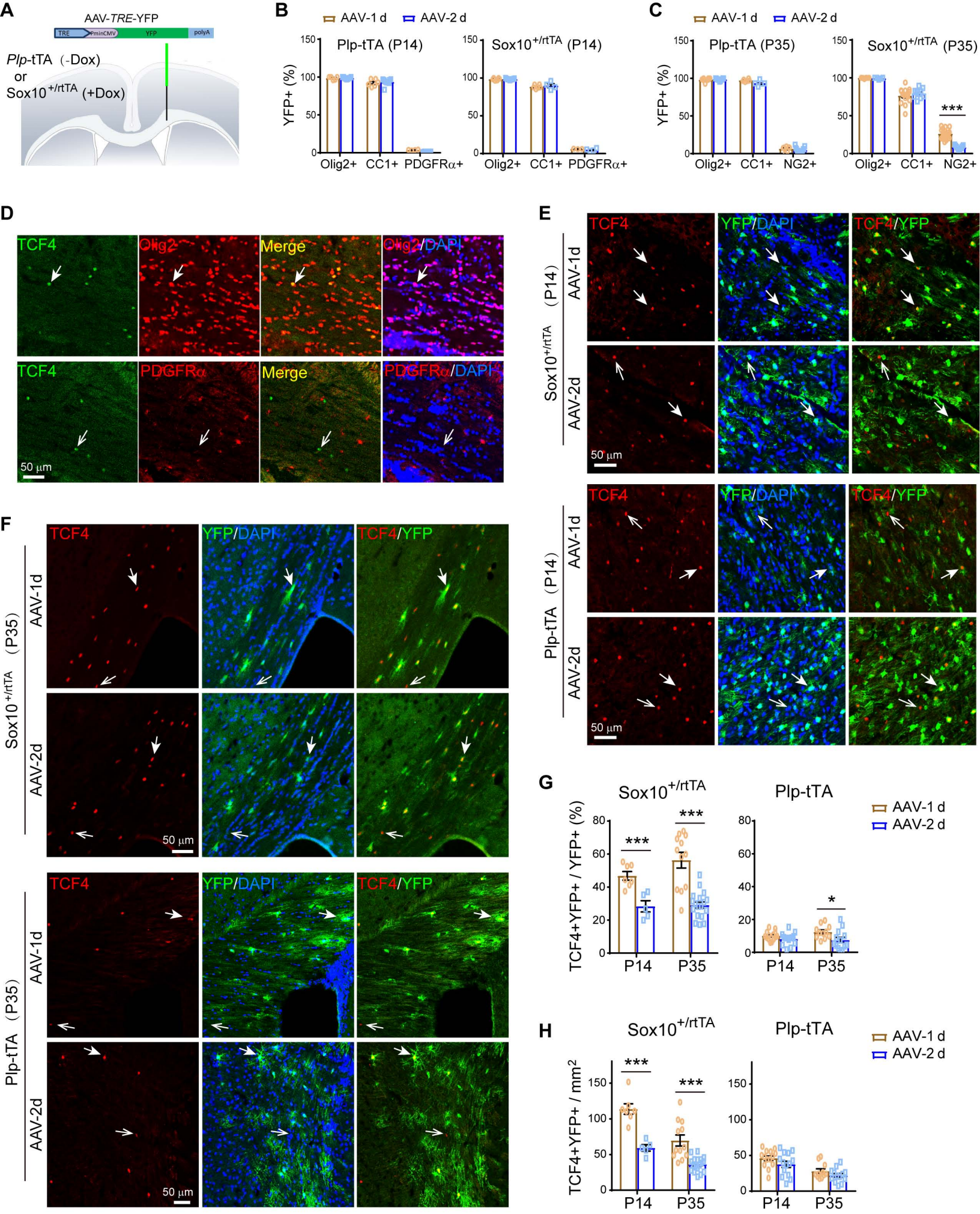
A
AAV-TRE-YFP
TRE
PminCMV
YFP
polyA
Plp-tTA (-Dox)
or
Sox10+/rtTA (+Dox)
B
AAV-1 d
AAV-2 d
Plp-tTA (P14)
Sox10+/rtTA (P14)
YFP+ (%)
Olig2+
CC1+
PDGFRα+
C
Plp-tTA (P35)
Sox10+/rtTA (P35)
NG2+
***
D
TCF4
Olig2
Merge
Olig2/DAPI
PDGFRα
PDGFRα/DAPI
50 μm
E
TCF4
YFP/DAPI
TCF4/YFP
Sox10+/rtTA (P14)
Plp-tTA (P14)
AAV-1d
AAV-2d
F
Sox10+/rtTA (P35)
Plp-tTA (P35)
G
TCF4+YFP+ / YFP+ (%)
P14
P35
*
H
TCF4+YFP+ / mm2

Figure 6

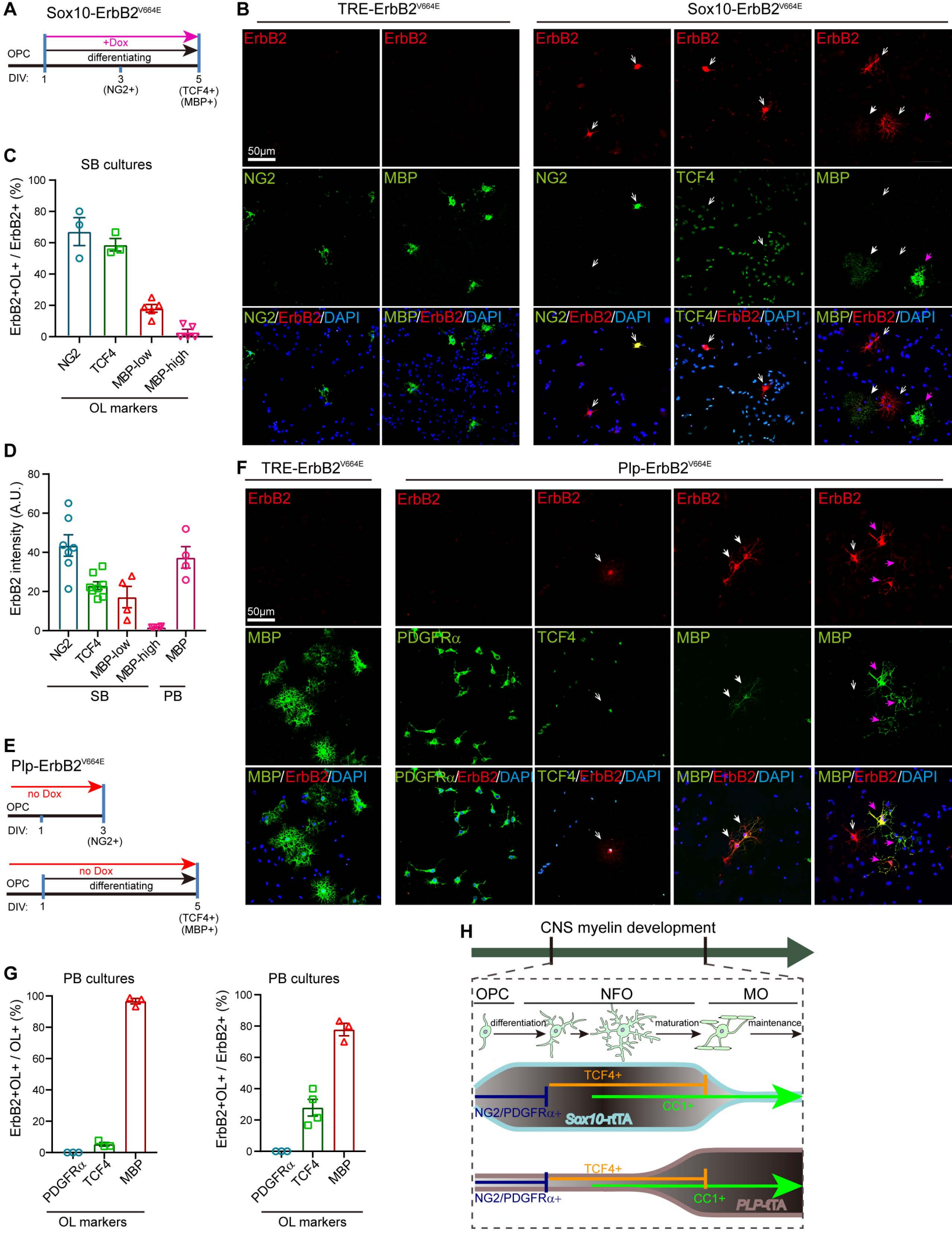
A
Sox10-ErbB2V664E
+Dox
OPC
differentiating
DIV: 1
3 (NG2+)
5 (TCF4+) (MBP+)
B
TRE-ErbB2V664E
Sox10-ErbB2V664E
ErbB2
50μm
NG2
MBP
TCF4
NG2/ErbB2/DAPI
MBP/ErbB2/DAPI
TCF4/ErbB2/DAPI
C
SB cultures
ErbB2+OL+ / ErbB2+ (%)
NG2
TCF4
MBP-low
MBP-high
OL markers
D
ErbB2 intensity (A.U.)
MBP
SB
PB
E
Plp-ErbB2V664E
no Dox
F
Plp-ErbB2V664E
PDGFRα
PDGFRα/ErbB2/DAPI
G
PB cultures
ErbB2+OL+ / OL+ (%)
ErbB2+OL+ / ErbB2+ (%)
H
CNS myelin development
OPC
NFO
MO
differentiation
maturation
maintenance
TCF4+
CC1+
NG2/PDGFRα+
Sox10-rtTA
PLP-rtTA

Figure 7

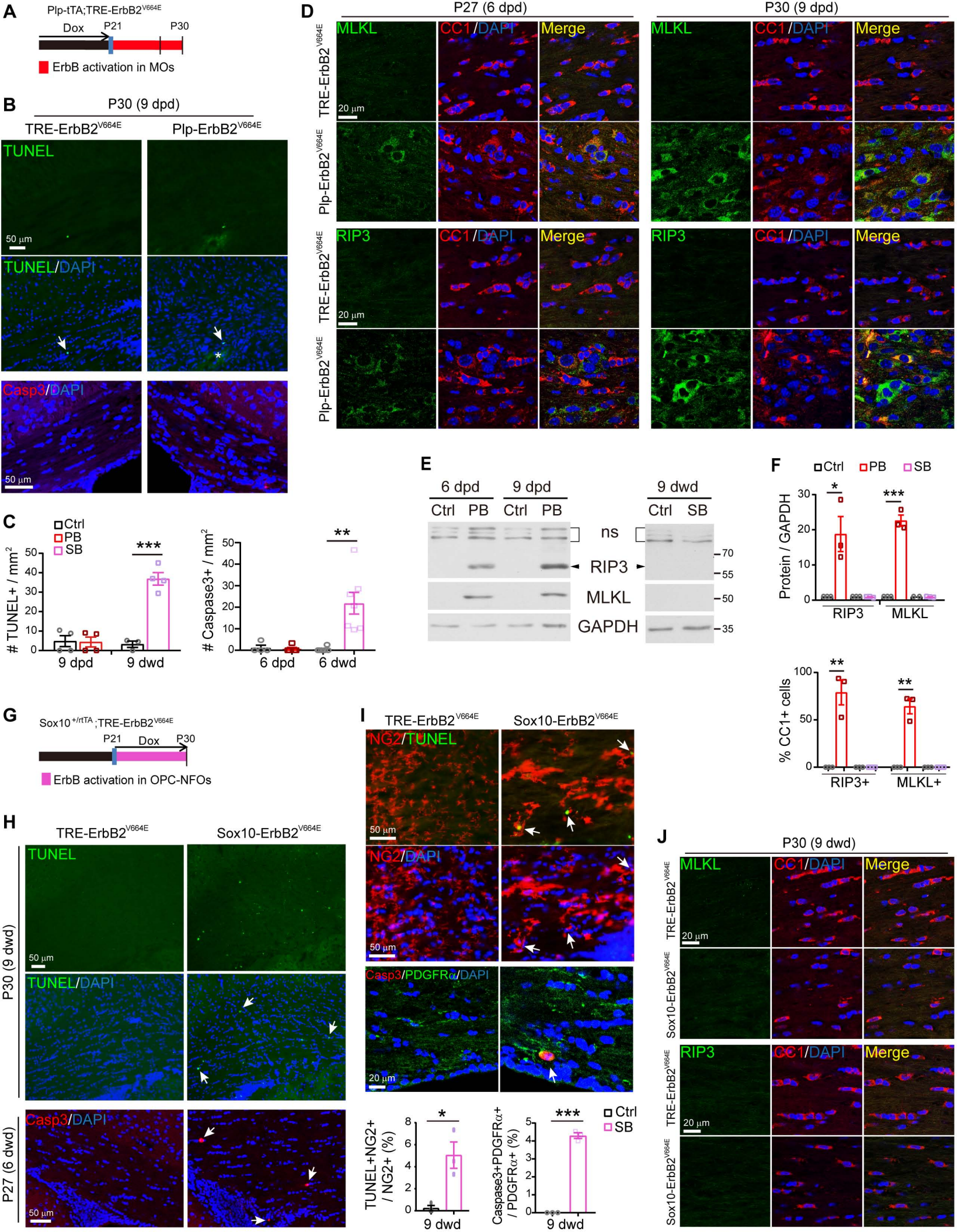
A
Plp-tTA;TRE-ErbB2V664E
Dox
P21
P30
ErbB activation in MOs
B
P30 (9 dpd)
TRE-ErbB2V664E
Plp-ErbB2V664E
TUNEL
TUNEL/DAPI
Casp3/DAPI
50 µm
C
Ctrl
PB
SB
TUNEL+ / mm2
Caspase3+ / mm2
9 dpd
9 dwd
6 dpd
6 dwd
D
P27 (6 dpd)
P30 (9 dpd)
MLKL
CC1/DAPI
Merge
RIP3
20 µm
E
6 dpd
9 dpd
9 dwd
Ctrl
PB
SB
ns
RIP3
MLKL
GAPDH
F
Protein / GAPDH
% CC1+ cells
RIP3
MLKL
RIP3+
MLKL+
G
Sox10+/rtTA;TRE-ErbB2V664E
P21
Dox
P30
ErbB activation in OPC-NFOs
H
TRE-ErbB2V664E
Sox10-ErbB2V664E
P30 (9 dwd)
P27 (6 dwd)
TUNEL
TUNEL/DAPI
Casp3/DAPI
I
NG2/TUNEL
NG2/DAPI
Casp3/PDGFRα/DAPI
TUNEL+NG2+ / NG2+ (%)
Caspase3+PDGFRα+ / PDGFRα+ (%)
J
P30 (9 dwd)
RIP3

Figure 8

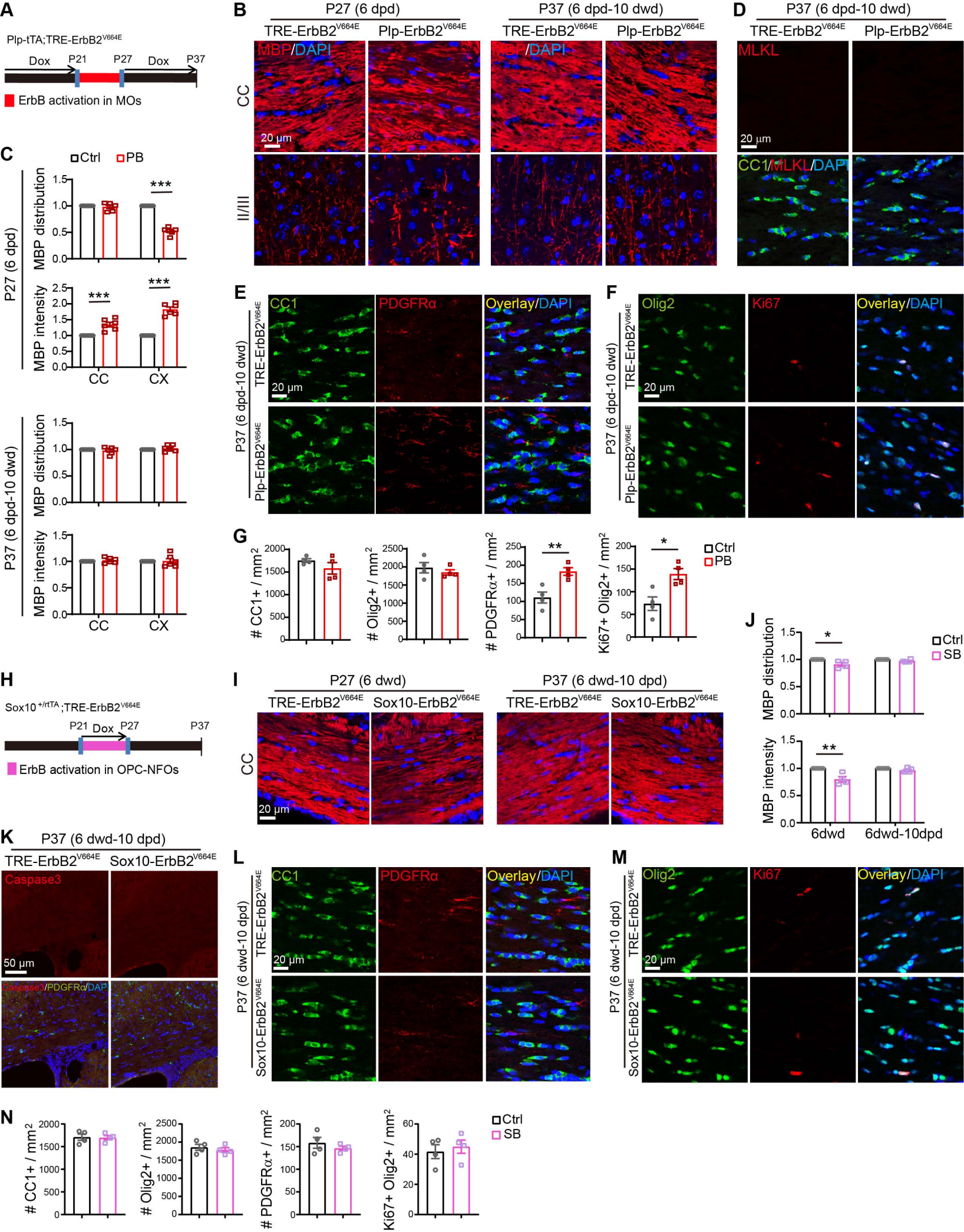
A
Plp-tTA;TRE-ErbB2V664E
Dox
P21
P27
Dox
P37
ErbB activation in MOs
B
P27 (6 dpd)
P37 (6 dpd-10 dwd)
TRE-ErbB2V664E
Plp-ErbB2V664E
MBP/DAPI
CC
II/III
20 μm
D
MLKL
CC1/MLKL/DAPI
C
Ctrl
PB
P27 (6 dpd)
MBP distribution
MBP intensity
***
CC
CX
P37 (6 dpd-10 dwd)
E
CC1
PDGFRα
Overlay/DAPI
F
Olig2
Ki67
G
CC1+ / mm2
Olig2+ / mm2
PDGFRα+ / mm2
Ki67+ Olig2+ / mm2
**
*
H
Sox10+/rtTA;TRE-ErbB2V664E
P21
Dox
P27
P37
ErbB activation in OPC-NFOs
I
P27 (6 dwd)
P37 (6 dwd-10 dpd)
Sox10-ErbB2V664E
J
SB
6dwd
6dwd-10dpd
K
Caspase3
Caspase3/PDGFRα/DAPI
50 μm
L
M
N

Figure 9

P21 (0 dpd)

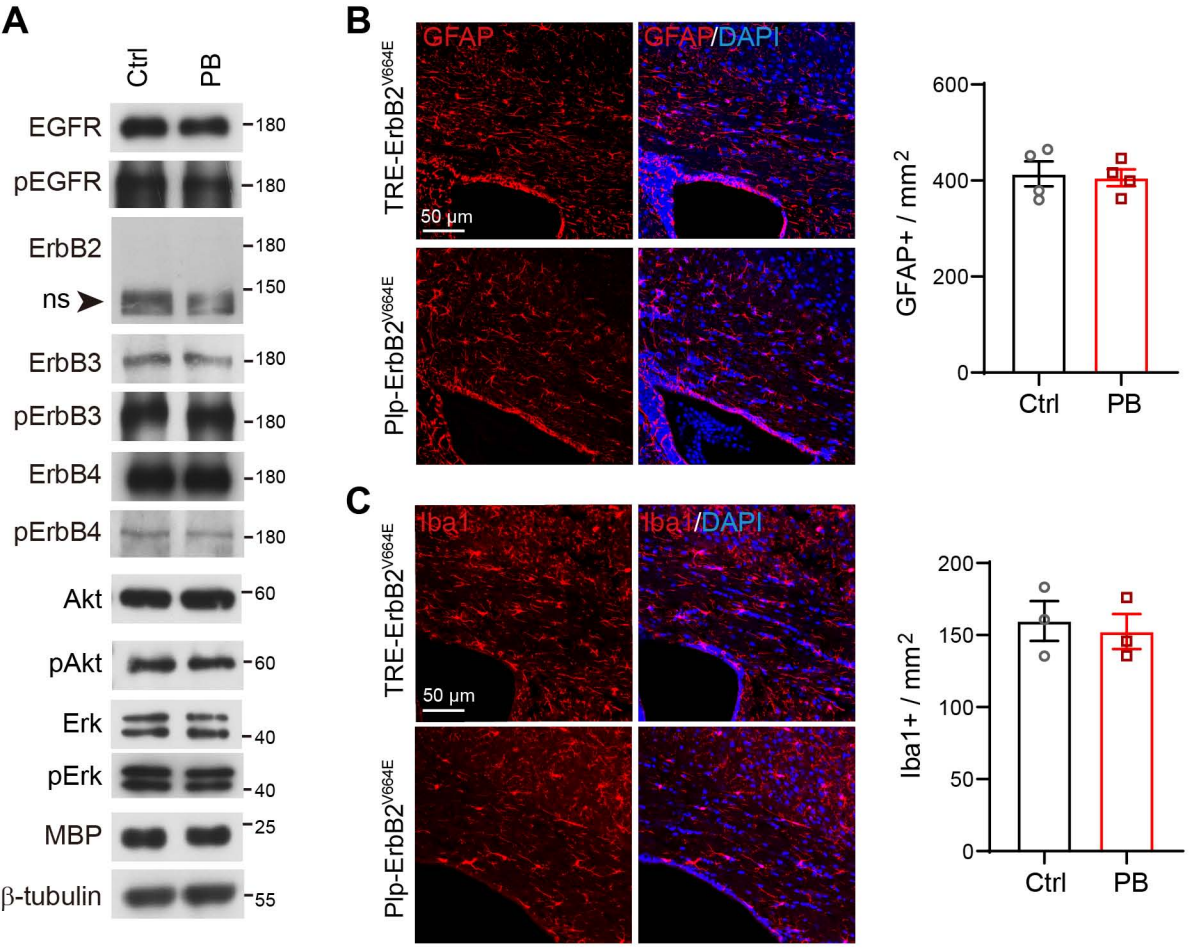

P21 (0 dwd)

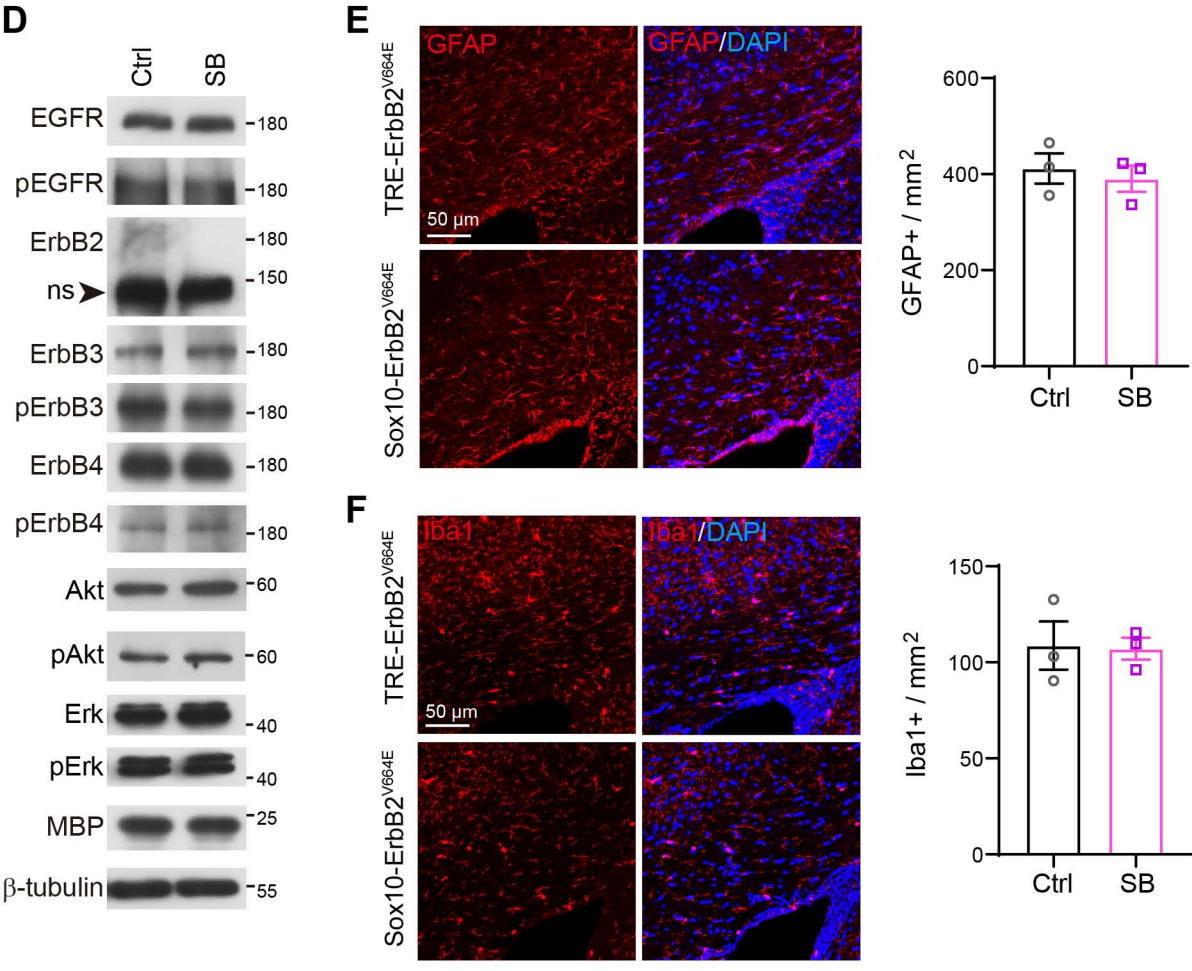

Extended data Figure 1-1

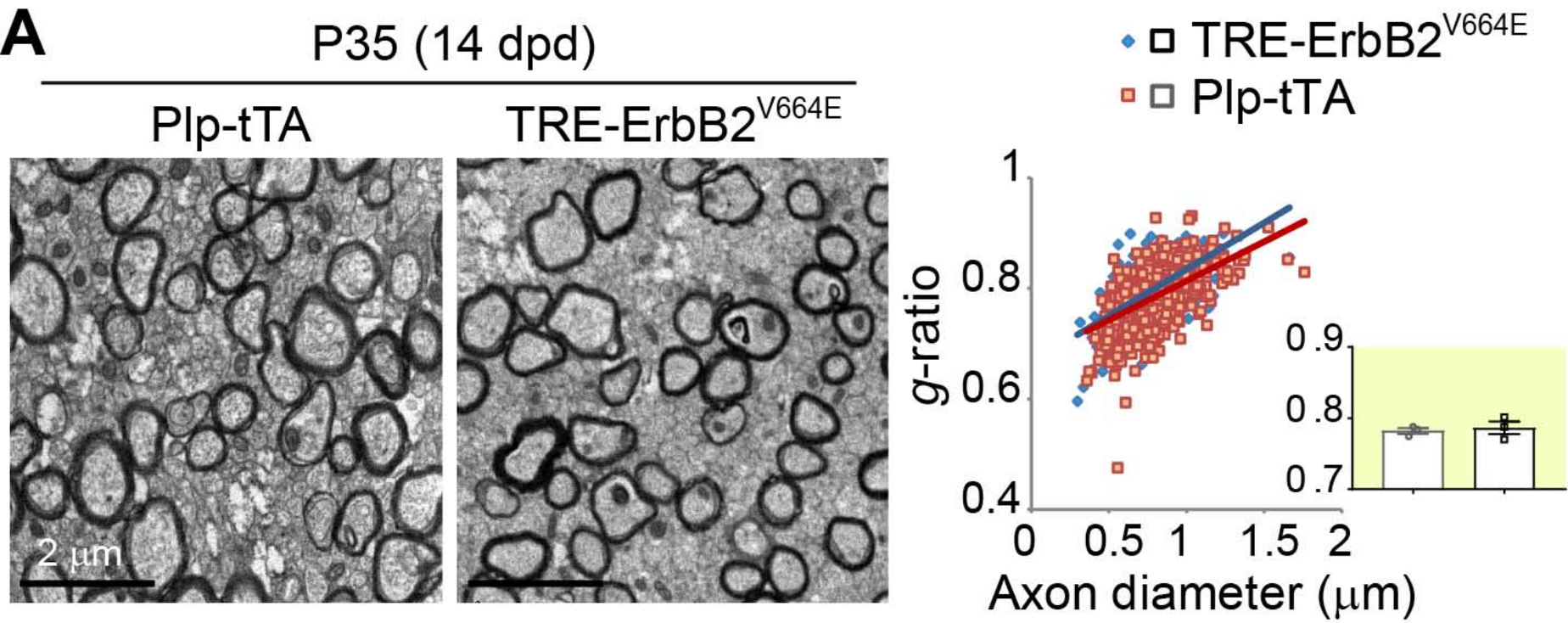

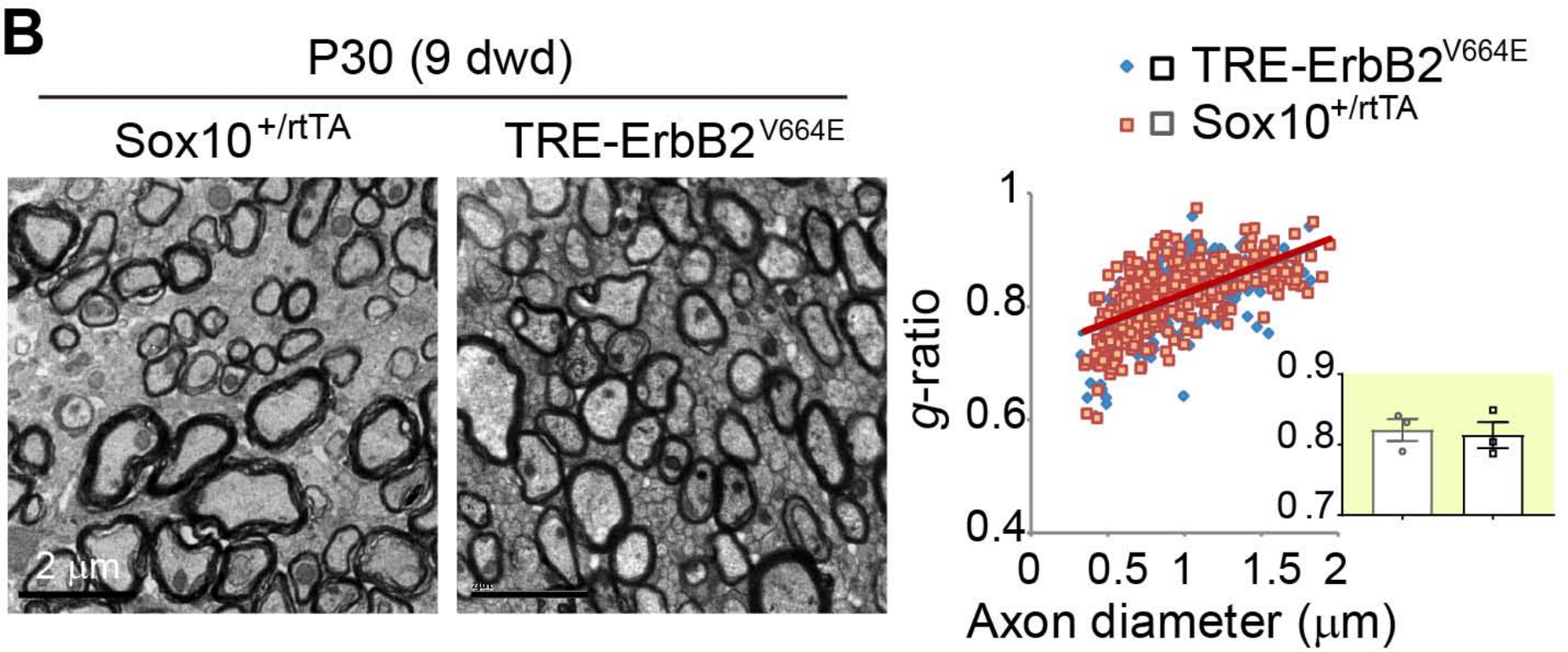

Extended data Figure 1-2

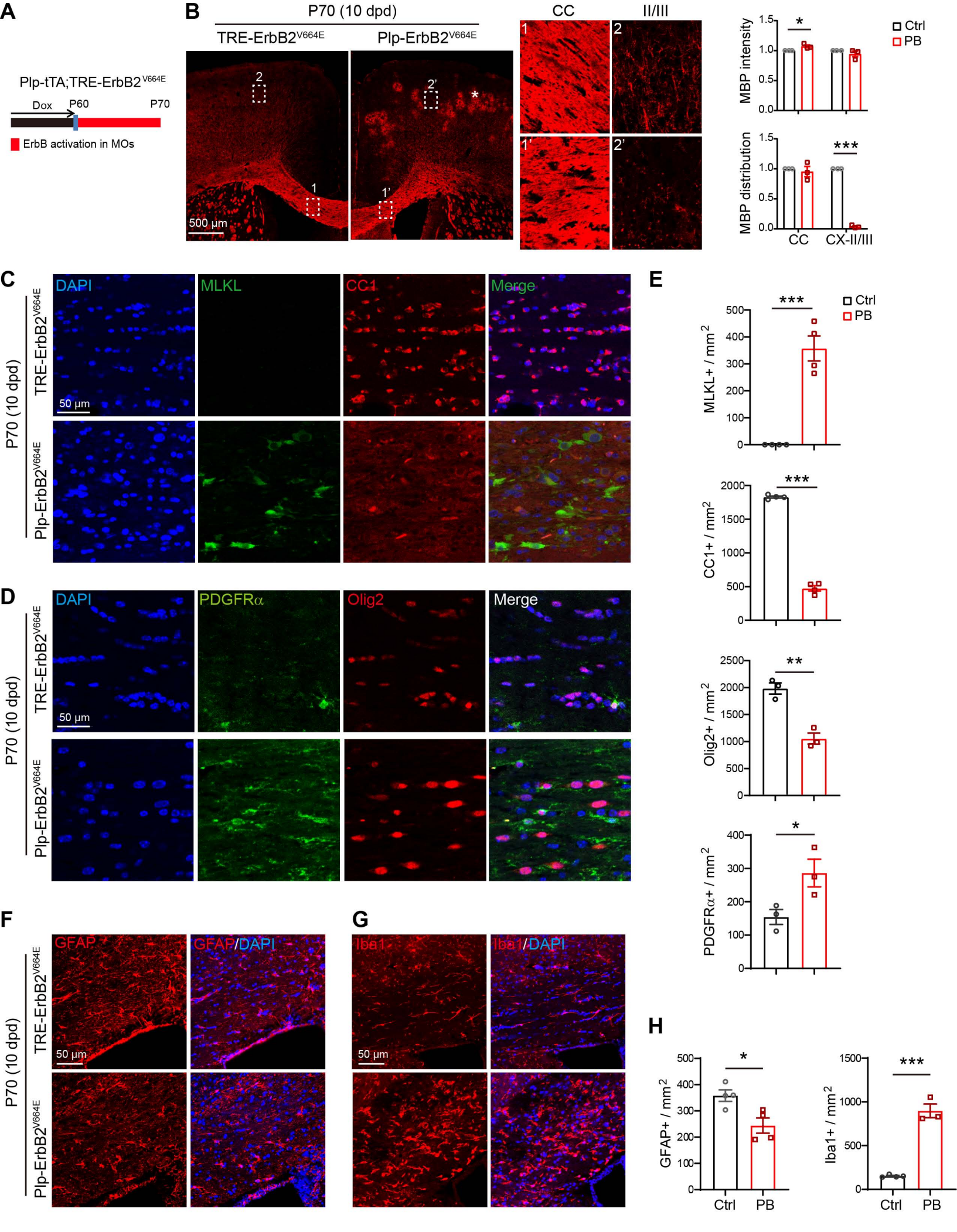

Extended data Figure 3-1

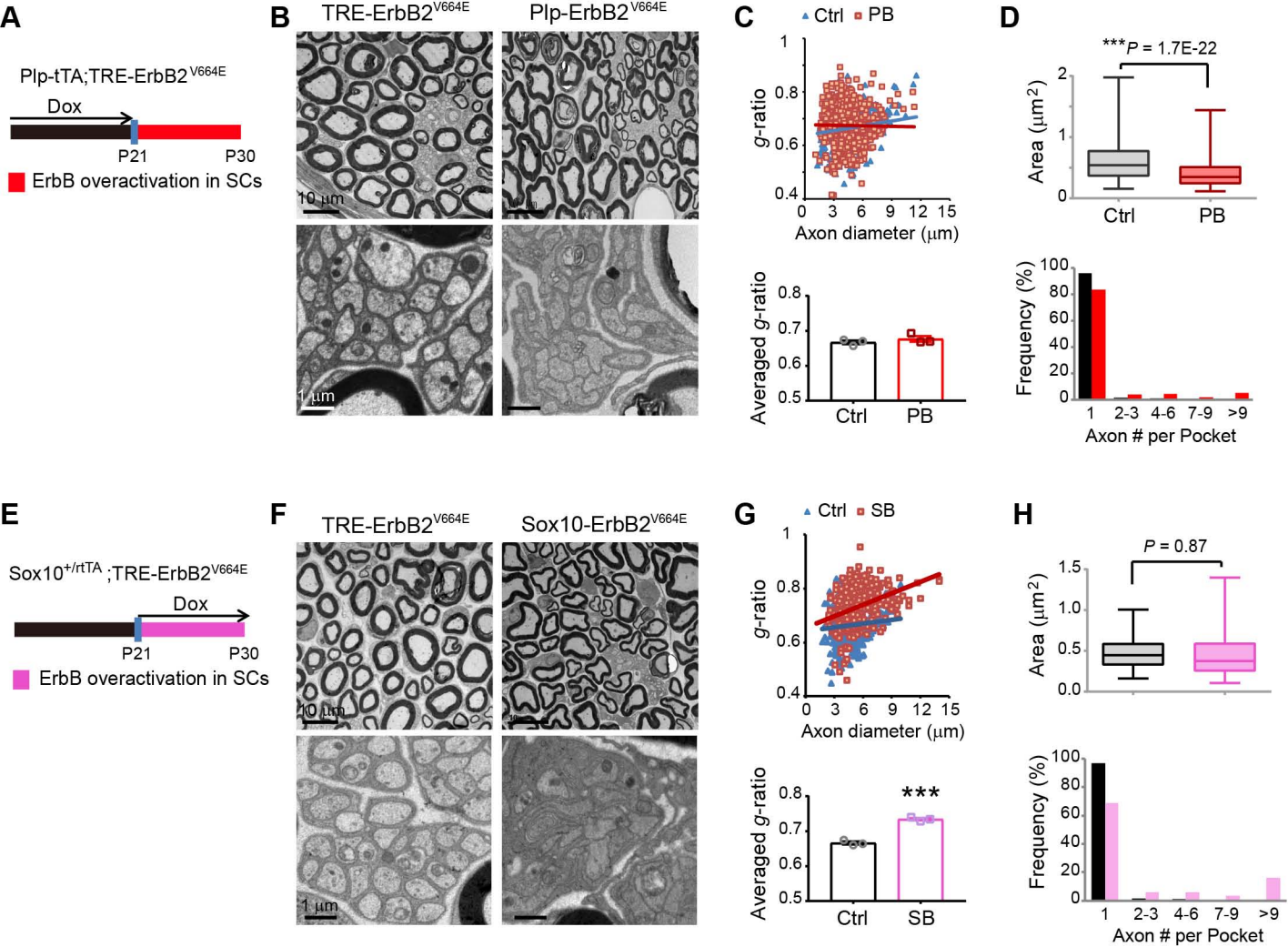

Extended data Figure 4-1

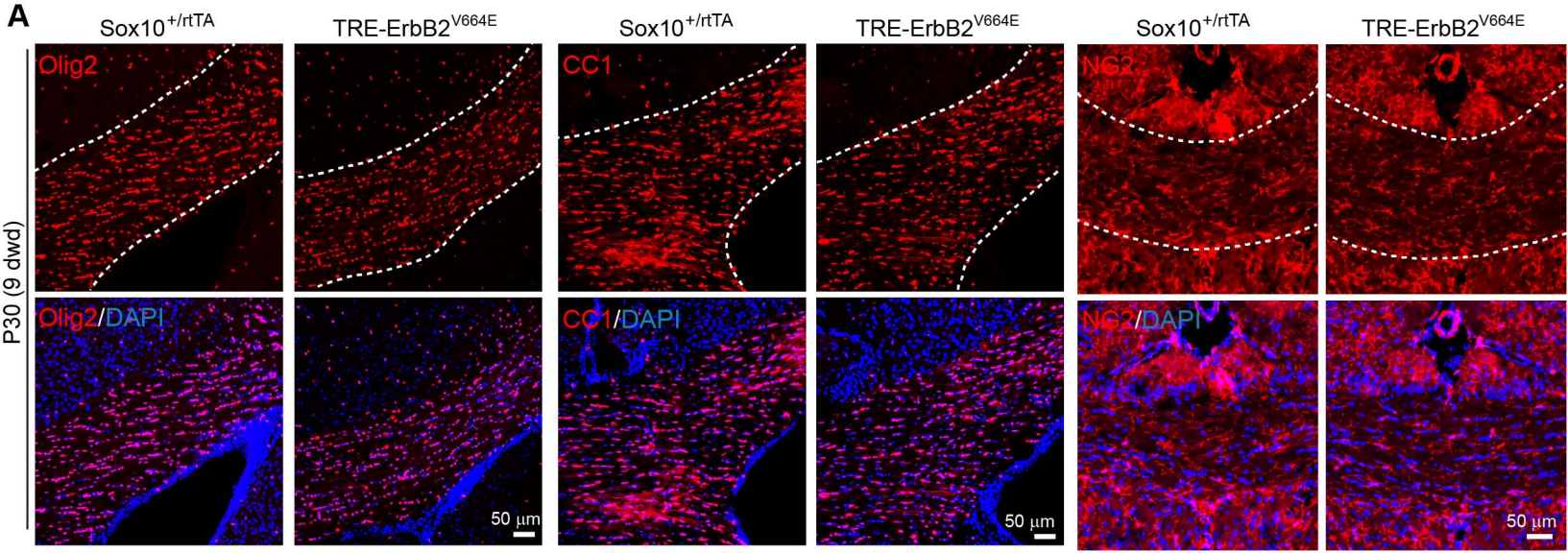

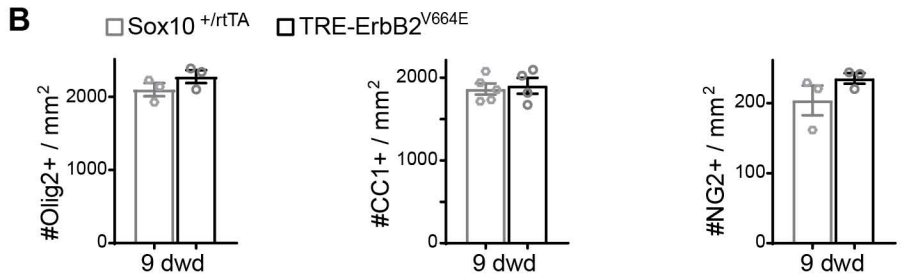

Extended data Figure 5-1

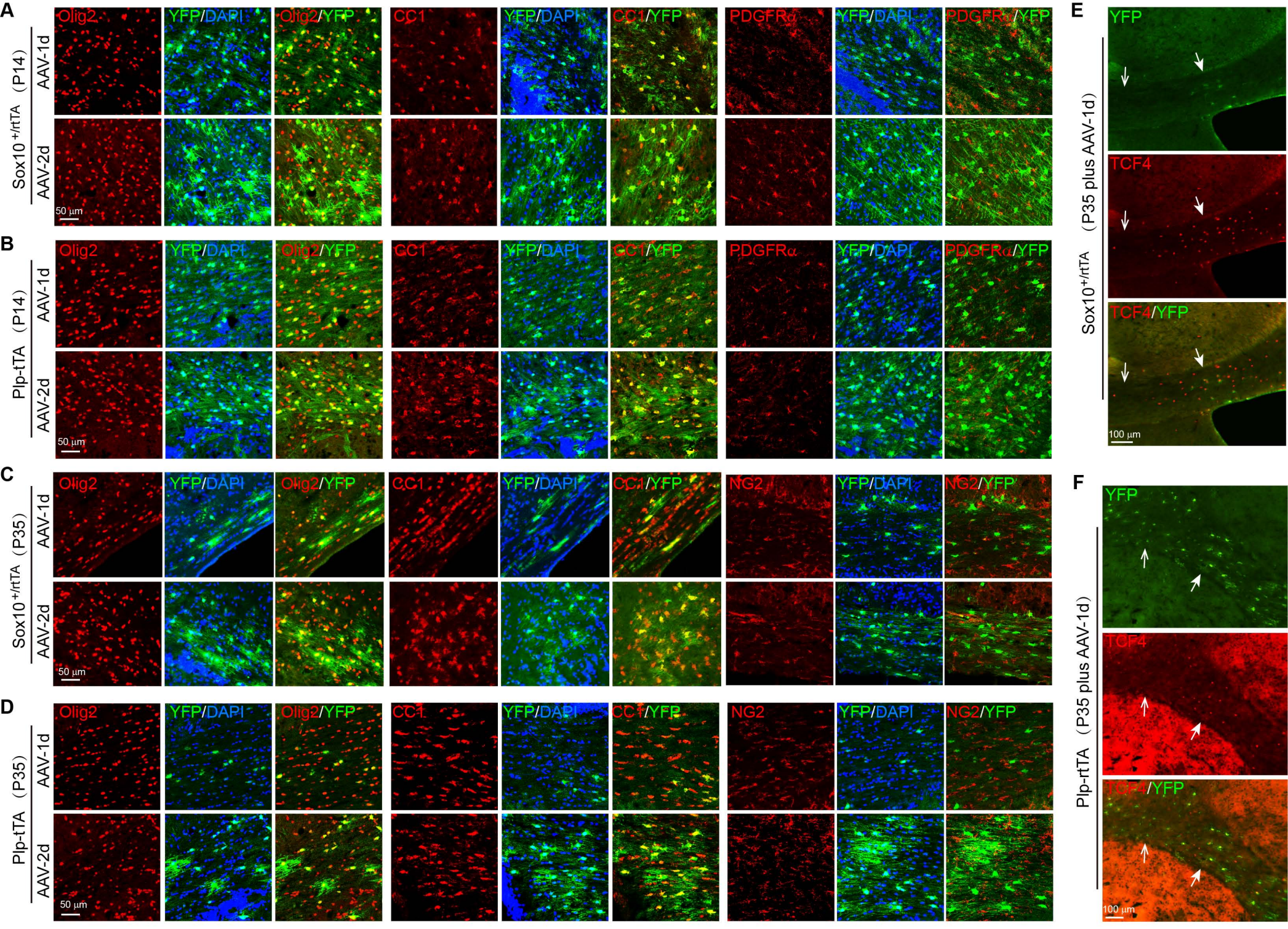

Extended data Figure 6-1